ELSEVIER

Journal of Fluids and Structures 22 (2006) 463–492

JOURNAL OF FLUIDS AND STRUCTURES

www.elsevier.com/locate/jfs

Second-order diffraction by a bottom-seated compound cylinder

S.A. Mavrakos, I.K. Chatjigeorgiou*

Division of Marine Structures, School of Naval Architecture and Marine Engineering, National Technical University of Athens, 9 Heroön Polytechniou Ave, Zografos Campus, GR157-73 Athens, Greece

Received 28 February 2005; accepted 7 December 2005
Available online 2 March 2006

Abstract

The second-order diffraction potential around a bottom-seated compound cylinder is considered. The solution method is based on a semi-analytical formulation for the double-frequency diffraction potentials, which are properly decomposed into a rational number of components in order to satisfy all boundary conditions involved in the problem. The solution process results in two different Sturm–Liouville problems which are treated separately in the ring-shaped fluid regions defined by the geometry of the structure. The matching of the potentials on the boundaries of adjacent fluid regions is established using the 'free' wave components of the potentials. Different Green's functions are constructed for each of the fluid regions surrounding the body. The calculation of integrals of the pressure distribution on the free surface is carried out using an appropriate Gauss–Legendre numerical technique. The efficiency of the method described in the present work is validated through comparative calculations. Finally, extensive numerical predictions are presented concerning the complete second-order excitation and the nonlinear wave elevation for various configurations of vertical axisymmetric bodies.
© 2006 Elsevier Ltd. All rights reserved.

1. Introduction

The solution of the second-order interaction problem between monochromatic and bichromatic waves and isolated or interacting bodies has attracted the attention of many researchers, especially during the past two decades. Significant improvements have been proposed in the literature to overcome the difficulties associated with the extensive numerical calculations which are required for the solution of the second-order velocity potential and subsequently the derivation of the nonlinear hydrodynamic loading and the free surface elevation. The afore-mentioned difficulties originate from the contribution of the second-order potential which has to satisfy the inhomogeneous boundary condition on the free surface. The solution process involves calculation of integrals in which the integrand exhibits strongly oscillatory behaviour.

The majority of the proposed solution methods which treat the problem of the second-order diffraction potential could be categorized into two major ensembles. The 'indirect' method was introduced independently by Lighthill (1979) for infinite water depth and Molin (1979) for finite water depth. According to this method, the calculation of the second-order potential is avoided by employing an 'assisting' first-order radiation potential. This method can be applied

*Corresponding author. Tel.: +30 210 772 1105; fax: +30 210 772 1412.
E-mail address: chatzi@naval.ntua.gr (I.K. Chatjigeorgiou).

0889-9746/$ - see front matter © 2006 Elsevier Ltd. All rights reserved.
doi:10.1016/j.jfluidstructs.2005.12.001

also for bodies with arbitrary shape and it was used thereafter by many researchers (Eatock Taylor and Hung, 1987; Abul-Azm and Williams, 1988, 1989a, b; Williams et al., 1990; Ghalayini and Williams, 1991; Mavrakos and Peponis, 1992; Moubayed and Williams, 1994, 1995; Liu et al., 1995; Rahman et al., 1999).

The second method, the so-called 'direct' method, allows the derivation of the second-order diffraction potential and subsequently the calculation of the pressure field around the body as well as the free surface elevation. The first attempt in that context was made by Loken (1986) for arbitrarily shaped bodies. Kim and Yue (1989, 1990) solved the second-order interaction problem between monochromatic and bichromatic incident waves and vertical bottom-seated axisymmetric bodies using the method of integral equations. The same method was used also by Chau and Eatock Taylor (1992). Huang and Eatock Taylor (1996) and Eatock Taylor and Huang (1997) developed a semi-analytical formulation for representing the second-order diffraction potential around truncated and bottom-seated cylinders, respectively. The solution presented by Teng and Kato (1999) was based on the integral representation of the fluid field, making use of an appropriate Green's function while at the same time they proposed an alternative method for calculating the integral on the free surface. Recently, Malenica et al. (1999) extended the semi-analytical formulation proposed by Huang and Eatock Taylor (1996) for calculating the second-order diffraction potential around arrays of vertical uniform bottom-fixed cylinders. They reported extensive numerical calculations concerning the hydrodynamic loading and the wave run-up in various multiple cylinder arrangements.

Although the problem of solving the second-order diffraction potential for uniform and truncated axisymmetric bodies is well treated in the literature, there is a lack of information for complex structures like compound cylinders. The present paper constitutes a contribution in this direction, and the subject of investigation is a two-part bottom-seated axisymmetric body. The main challenge that must be treated in the particular configuration is that the inhomogeneous boundary condition should be satisfied in two fluid regions in the radial direction. The two second-order diffraction potentials should subsequently be matched along the boundaries of these regions. The satisfaction of all boundary conditions involved in the problem and the matching of the potentials is accomplished by defining a 'locked' and a 'free' wave potential in the outer field and a 'trapped' wave as well as a corresponding 'free' wave potential in the upper inner field. The matching of the potentials is performed using the 'free' wave components. The solution method is based on the semi-analytical expansion formulation proposed by Huang and Eatock Taylor (1996), which is extended in the present analysis to represent the complete second-order diffraction potential in the upper inner field as well. It should also be noted that although the body which is studied is fixed on the bottom, the inhomogeneous term of the nonlinear free surface condition is used in its general form. Therefore, the specific formulation can be appropriately extended for floating compound cylinders.

2. Formulation of the second-order problem for a bottom-seated compound cylinder

We consider a vertical compound axisymmetric body exposed to the action of a monochromatic incident wave of frequency ω and linear amplitude $H/2$. The body, for which the main dimensions are given in Fig. 1, is fixed in water of depth h. A cylindrical coordinate system (r, θ, z) is chosen, with its origin on the sea bed and its Oz axis pointing vertically upwards.

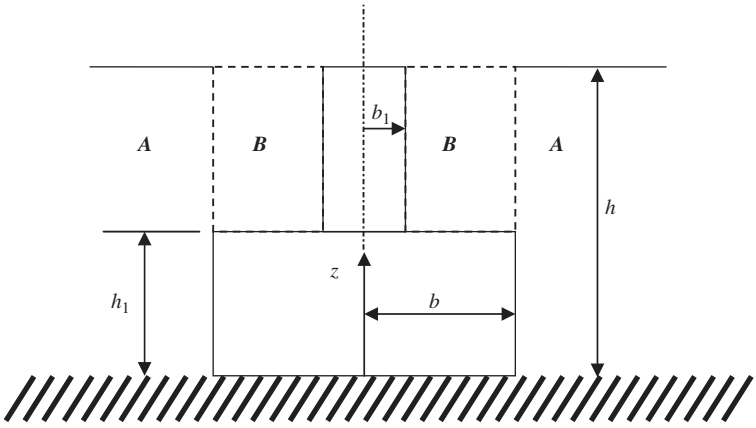

Fig. 1. Bottom-seated compound cylinder: main dimensions and fluid regions.

The total second-order velocity potential can be written as

$$\phi_2(r,\theta,z;t) = \mathscr{R}e\{\varphi_2(r,\theta,z)e^{-2i\omega t}\}. \tag{1}$$

The spatially dependent counterpart $\varphi_2(r,\ \theta,\ z)$ should satisfy the Laplace equation in the whole fluid region surrounding the body,

$$\nabla^2\varphi_2 = 0 \text{ in} \begin{cases} b \leqslant r, & 0 \leqslant z \leqslant h, \\ b_1 \leqslant r \leqslant b, & h_1 \leqslant z \leqslant h \end{cases} \tag{2}$$

and the following boundary conditions:

$$\left(\frac{\partial\varphi_2}{\partial z}\right)_{z=0} = 0, \quad b \leqslant r, \tag{3}$$

$$\left(\frac{\partial\varphi_2}{\partial z}\right)_{z=h_1} = 0, \quad b_1 \leqslant r \leqslant b, \tag{4}$$

$$\left(-4\nu\varphi_2 + \frac{\partial\varphi_2}{\partial z}\right)_{z=h} = q(r,\theta), \quad b_1 \leqslant r, \tag{5}$$

$$\left(\frac{\partial\varphi_2}{\partial r}\right)_{r=b} = 0, \quad 0 \leqslant z \leqslant h_1, \tag{6}$$

$$\left(\frac{\partial\varphi_2}{\partial r}\right)_{r=b_1} = 0, \quad h_1 \leqslant z \leqslant h, \tag{7}$$

where $\nu = \omega^2/g$. Furthermore $q(r,\theta)$ is the effective pressure distribution on the free surface, which is expressed as

$$q(r,\theta) = \frac{i\omega}{g}\left[2\frac{\partial\varphi_1^I}{\partial r}\frac{\partial\varphi_1^D}{\partial r} + \frac{2}{r^2}\frac{\partial\varphi_1^I}{\partial\theta}\frac{\partial\varphi_1^D}{\partial\theta} + \left(3\nu^2 - \frac{\kappa^2}{2}\right)\varphi_1^I\varphi_1^D - \frac{1}{2}\varphi_1^I\frac{\partial^2\varphi_1^D}{\partial z^2} + \frac{\partial\varphi_1^D}{\partial r}\frac{\partial\varphi_1^D}{\partial r} + \frac{1}{r^2}\frac{\partial\varphi_1^D}{\partial\theta}\frac{\partial\varphi_1^D}{\partial\theta} + \frac{3}{2}\nu^2\varphi_1^D\varphi_1^D - \frac{1}{2}\varphi_1^D\frac{\partial^2\varphi_1^D}{\partial z^2}\right]_{z=h} + q_{II}, \tag{8}$$

where q_{II} expresses the contribution from the quadratic products of the first-order incident wave potential. The wavenumber κ is derived through the imaginary solution $a_0 = -i\kappa$ of the first-order transcendental equation

$$a_j \tan(a_j h) + \nu = 0, \tag{9}$$

which in turn leads to the corresponding first-order dispersion equation

$$\kappa \tanh(\kappa h) = \nu. \tag{10}$$

In Eq. (8), φ_1^I and φ_1^D denote the first-order incident wave and diffraction potentials, respectively. A suitable way to express the effective pressure distribution is the following (Chau and Eatock Taylor, 1992):

$$q(r,\theta) = \sum_{m=-\infty}^{\infty} q_m(r)e^{im\theta}. \tag{11}$$

The fundamentals of the method described herein for the solution of the second-order diffraction problem of the compound cylinder under consideration are similar to those applied for the solution of the first-order problem. Thus, the fluid field is separated into ring-type regions denoted by ***A*** and ***B*** (Fig. 1) and different first- and second-order velocity potentials are defined for each region. The second-order diffraction problem in each of these regions is treated separately, and eventually the solution methodology is accomplished by matching the potentials along the cylindrical boundary on $r = b$.

2.1. Second-order velocity potential for field B

The total second-order diffraction potential in field ***B***, φ_{2B}, should satisfy the Laplace equation and the following boundary conditions which are obtained by the generic Eqs. (3)–(7):

$$\left(\frac{\partial\varphi_{2B}}{\partial z}\right)_{z=h_1} = 0, \quad b_1 \leqslant r \leqslant b, \tag{12}$$

$$\left(-4\nu\varphi_{2B}+\frac{\partial\varphi_{2B}}{\partial z}\right)_{z=h}=q_B(r,\theta),\quad b_1\leqslant r\leqslant b, \tag{13}$$

$$\left(\frac{\partial\varphi_{2B}}{\partial r}\right)_{r=b_1}=0,\quad h_1\leqslant z\leqslant h, \tag{14}$$

where the effective pressure distribution $q_B(r,\theta)$ is given by Eq. (8) in which, in lieu of φ_1^D, the first-order diffraction potential φ_{1B}^D is used.

Furthermore, φ_{2B} and the total second-order velocity potential in the outer field $\boldsymbol{A}$, φ_{2A}, should satisfy the following matching conditions on the boundary between fields $\boldsymbol{A}$ and $\boldsymbol{B}$:

$$\frac{\partial\varphi_{2B}}{\partial r}=\frac{\partial\varphi_{2A}}{\partial r},\ r=b,\quad h_1\leqslant z\leqslant h \tag{15}$$

and

$$\varphi_{2B}=\varphi_{2A},\quad r=b,\quad h_1\leqslant z\leqslant h. \tag{16}$$

In order to properly satisfy boundary conditions (12)–(14), φ_{2B} is decomposed into two components according to

$$\varphi_{2B}=\varphi_{2B}^{ID}+\varphi_{2B}^{DD}. \tag{17}$$

It should be noted that Eq. (17) includes the influence of second-order incident waves.

Both parts on the right-hand side of Eq. (17) satisfy individually the Laplace equation in the entire field $\boldsymbol{B}$ and the zero velocity condition on the horizontal step $z=h_1$. Thus,

$$\nabla^2\varphi_{2B}^{ID}=0,\quad \nabla^2\varphi_{2B}^{DD}=0,\quad b_1\leqslant r\leqslant b,\quad h_1\leqslant z\leqslant h \tag{18a,b}$$

and

$$\left(\frac{\partial\varphi_{2B}^{ID}}{\partial z}\right)_{z=h_1}=0,\quad \left(\frac{\partial\varphi_{2B}^{DD}}{\partial z}\right)_{z=h_1}=0,\quad b_1\leqslant r\leqslant b. \tag{19a,b}$$

Also, both components have to satisfy the zero velocity condition on the structure for $r=b_1$:

$$\left(\frac{\partial\varphi_{2B}^{ID}}{\partial r}\right)_{r=b_1}=0,\quad \left(\frac{\partial\varphi_{2B}^{DD}}{\partial r}\right)_{r=b_1}=0,\quad h_1\leqslant r\leqslant h. \tag{20a,b}$$

Concerning the free-surface boundary condition (13) for the components φ_{2B}^{ID} and φ_{2B}^{DD}, they are expressed using the following homogeneous and inhomogeneous relations, respectively:

$$\left(-4\nu\varphi_{2B}^{ID}+\frac{\partial\varphi_{2B}^{ID}}{\partial z}\right)_{z=h}=0,\quad b_1\leqslant r\leqslant b, \tag{21}$$

$$\left(-4\nu\varphi_{2B}^{DD}+\frac{\partial\varphi_{2B}^{DD}}{\partial z}\right)_{z=h}=q_B(r,\theta),\quad b_1\leqslant r\leqslant b. \tag{22}$$

Before we proceed to the explanation of the solution methodology, it is advisable to provide some important information regarding the calculation of the effective pressure distribution $q_B(r,\theta)$. In Eq. (8) which is used for expressing $q_B(r,\theta)$, the subscript 1 denotes the first-order velocity potential, while superscripts I and D denote the incident and the diffraction components, respectively. In the present study, the total first-order velocity potential—including both incident and diffracted wave fields—in the fluid region $\boldsymbol{B}$ is derived in the form proposed by Mavrakos and Koumoutsakos (1987):

$$\varphi_{1B}=-\mathrm{i}\omega\frac{H}{2}\sum_{m=-\infty}^{\infty}\mathrm{i}^m\Psi_m^{(1B)}(r,z)\mathrm{e}^{\mathrm{i}m\theta}, \tag{23}$$

$$\frac{1}{h}\Psi_m^{(1B)}(r,z)=\sum_{j=0}^{\infty}F_{mj}^{(1B)}R_{mj}^{(1B)}(r)\,Y_j(z), \tag{24}$$

where

$$R_{mj}^{(1B)}(r) = R_{mj}(r) - \frac{R'_{mj}(b_1)}{R'^{*}_{mj}(b_1)} R^{*}_{mj}(r), \tag{25}$$

$$R_{mj}(r) = \frac{\mathrm{K}_m(\mu_j b_1)\mathrm{I}_m(\mu_j r) - \mathrm{I}_m(\mu_j b_1)\mathrm{K}_m(\mu_j r)}{\mathrm{I}_m(\mu_j b)\mathrm{K}_m(\mu_j b_1) - \mathrm{I}_m(\mu_j b_1)\mathrm{K}_m(\mu_j b)}, \tag{26}$$

$$R^{*}_{mj}(r) = \frac{\mathrm{I}_m(\mu_j b)\mathrm{K}_m(\mu_j r) - \mathrm{K}_m(\mu_j b)\mathrm{I}_m(\mu_j r)}{\mathrm{I}_m(\mu_j b)\mathrm{K}_m(\mu_j b_1) - \mathrm{I}_m(\mu_j b_1)\mathrm{K}_m(\mu_j b)}. \tag{27}$$

Moreover, I_m and K_m are the mth order modified Bessel functions of the first- and second kind, respectively, and $Y_j(z)$ are orthonormal functions in $[h_1,h]$ defined by

$$Y_0(z) = M_0^{-1/2}\cosh(\kappa_B(z-h_1)), \tag{28}$$

$$Y_j(z) = M_j^{-1/2}\cos(\mu_j(z-h_1)) \quad \text{for } j \geqslant 1, \tag{29}$$

$$M_0 = \frac{1}{2}\left[1 + \frac{\sinh(2\kappa_B(h-h_1))}{2\kappa_B(h-h_1)}\right], \tag{30}$$

$$M_j = \frac{1}{2}\left[1 + \frac{\sin(2\mu_j(h-h_1))}{2\mu_j(h-h_1)}\right] \quad \text{for } j \geqslant 1, \tag{31}$$

where μ_j are the roots of the transcendental equation

$$\nu + \mu_j \tan(\mu_j(h-h_1)) = 0. \tag{32}$$

Eq. (32) has an infinite number of real roots for $j \geqslant 1$ and one imaginary root $\mu_0 = -\mathrm{i}\kappa_B$, which leads to the first-order dispersion equation for the upper inner field $\boldsymbol{B}$

$$\kappa_B \tanh(\kappa_B(h-h_1)) = \nu. \tag{33}$$

Since φ_{1B} along with $\Psi_m^{(1B)}(r,z)$ (see Eqs. (23) and (24), respectively) denote the total linear velocity potential in $\boldsymbol{B}$, for calculating the inhomogeneous term in Eq. (22), the diffraction potential will be delivered from Eq. (23) after subtracting the first-order incident wave.

It can be shown that the effective pressure distribution $q_B(r,\theta)$ in $\boldsymbol{B}$ can be written in accordance with Eq. (11) as

$$q(r,\theta)\big|_{z=h} = \sum_{m=-\infty}^{\infty} q_m^{(B)}(r)\mathrm{e}^{\mathrm{i}m\theta}, \quad q_m^{(B)}(r) = -\mathrm{i}\omega\left(\frac{H}{2}\right)^2 \frac{1}{h}\,\mathrm{i}^m Q_m^{(B)}(r). \tag{34a,b}$$

The radial function $Q_m^{(B)}(r)$ is nondimensionalized.

In order to allow at a later stage the matching of potentials in fields $\boldsymbol{B}$ and $\boldsymbol{A}$ along their common boundary on $r = b$, we assume that φ_{2B}^{DD} satisfies

$$\left(\frac{\partial\varphi_{2B}^{DD}}{\partial r}\right)_{r=b} = 0, \quad h_1 \leqslant z \leqslant h. \tag{35}$$

In other words the velocity field that is described by φ_{2B}^{DD} represents a 'trapped' wave component in the fluid annulus that radially extends between b_1 and b. The equation of the radial velocities and potentials along the boundary of fields $\boldsymbol{A}$ and $\boldsymbol{B}$, is incorporated into the formulation through proper evaluation of φ_{2B}^{ID}. This will be discussed in Section 2.3.

2.2. Second-order 'trapped' wave potential φ_{2B}^{DD} due to free surface forcing

According to the preceding analysis, there is sufficient material for the discrete evaluation of the 'trapped' wave potential. The governing system to be considered consists of Eqs. (18b), (19b), (20b), (22) and (35). A general expression that satisfies Eqs. (19b) and (22) is given by

$$\varphi_{2B}^{DD}(r,\theta,z) = \frac{\cosh(\beta(z-h_1))}{\nu\cosh(\beta(h-h_1))}\sum_{m=-\infty}^{\infty} q_m^{(B)}(r)\mathrm{e}^{\mathrm{i}m\theta} + \sum_{m=-\infty}^{\infty}\sum_{j=0}^{\infty} \mathrm{R}_{mj}(r)\,Y_j^{(2)}(z)\mathrm{e}^{\mathrm{i}m\theta}, \tag{36}$$

where

$$\beta \tanh(\beta(h-h_1)) = 5v, \tag{37}$$

$$4v + \sigma_j \tan(\sigma_j(h-h_1)) = 0, \tag{38}$$

while $Y_j^{(2)}(z)$ are orthonormal functions in $[h_1,h]$ given by

$$Y_j^{(2)}(z) = \left(M_j^{(2)}\right)^{-1/2} \cos(\sigma_j(z-h_1)), \tag{39}$$

$$M_j^{(2)} = \frac{1}{2}\left[1 + \frac{\sin(2\sigma_j(h-h_1))}{2\sigma_j(h-h_1)}\right]. \tag{40}$$

By analogy to the first-order transcendental Eq. (32), Eq. (38) has an infinite number of real roots for $j \geqslant 1$ and one imaginary root $\sigma_0 = -i\rho_B$ given by the second-order dispersion equation

$$\rho_B \tanh(\rho_B(h-h_1)) = 4v. \tag{41}$$

In this special case, the orthonormal functions will be given by

$$Y_0^{(2)}(z) = \left(M_0^{(2)}\right)^{-1/2} \cosh(\rho_B(z-h_1)), \tag{42}$$

$$M_0^{(2)} = \frac{1}{2}\left[1 + \frac{\sinh(2\rho_B(h-h_1))}{2\rho_B(h-h_1)}\right]. \tag{43}$$

Eq. (36) is introduced into the Laplace Eq. (18b). After equating terms of the same order m and making use of the eigenfunction expansion technique in the z direction, the following is derived:

$$\frac{\mathrm{d}^2\Phi_{mj}(r)}{\mathrm{d}r^2} + \frac{1}{r}\frac{\mathrm{d}\Phi_{mj}(r)}{\mathrm{d}r} - \left(\frac{m^2}{r^2} + \sigma_j^2\right)\Phi_{mj}(r) + B_j q_m^{(B)}(\beta^2 + \sigma_j^2) = 0, \tag{44}$$

where

$$\Phi_{mj}(r) = \mathrm{R}_{mj}(r) + B_j q_m^{(B)}(r), \tag{45}$$

$$B_j = \frac{1}{h-h_1}\int_{h_1}^{h} \frac{\cosh(\beta(z-h_1))}{v\cosh(\beta(h-h_1))}\, Y_j^{(2)}(z)\,\mathrm{d}z = \frac{1}{h-h_1}\frac{1}{\sigma_j^2+\beta^2}\, Y_j^{(2)}(h). \tag{46}$$

In order to calculate $\Phi_{mj}(r)$, we consider the following Sturm–Liouville problem which is obtained after rearranging terms in Eq. (44):

$$(r\Phi'_{mj}(r))' - \left(\frac{m^2}{r} + \sigma_j^2 r\right)\Phi_{mj}(r) = -\frac{r}{h-h_1}\, Y_j^{(2)}(h) q_m^{(B)}(r), \quad b_1 \leqslant r \leqslant \mathrm{d}, \tag{47}$$

where the primes denote differentiation with respect to radius r. Next, we seek a solution of the form

$$\Phi_{mj}(r) = \frac{Y_j^{(2)}(h)}{h-h_1}\int_{b_1}^{b} \xi q_m^{(B)}(\xi) G_{mj}^{(B)}(r;\xi)\,\mathrm{d}\xi, \tag{48}$$

where $G_{mj}^{(B)}(r;\xi)$ is the one-dimensional Green's function.

Construction of Green's function for the 'trapped' wave component

The first property of Green's function is that it satisfies the corresponding homogeneous problem

$$\left(rG'^{(B)}_{mj}\right)' - \left(\frac{m^2}{r} + \sigma_j^2 r\right) G_{mj}^{(B)} = 0. \tag{49}$$

G_{mj} must be continuous at $r = \xi$ and G_{mj}' must be discontinuous at $r = \xi$, with a discontinuity of

$$G'_{mj}(r;r+) - G'_{mj}(r;r-) = -\frac{1}{r}. \tag{50}$$

Finally, $G_{mj}^{(B)}$ must satisfy the boundary conditions of $\Phi_{mj}(r)$ on boundaries $r = b_1$ and $r = b$. Thus, $G'^{(B)}_{mj}$ must be equal to zero for $r = b_1$ and $r = b$.

Note that Eq. (49) is the modified Bessel equation. The properties of Green's function (Hildebrand, 1962; Dettman, 1988) and the boundary conditions at $r = b_1$ and $r = b$ are applied to the solution of Eq. (49), i.e. to the modified Bessel Functions I and K, to give

$$G_{mj}^{(B)}(r;\xi) = \frac{1}{\gamma_{mj} - \delta_{mj}}[\mathrm{I}_m(\sigma_j r) - \delta_{mj}\mathrm{K}_m(\sigma_j r)] \cdot [\mathrm{I}_m(\sigma_j \xi) - \gamma_{mj}\mathrm{K}_m(\sigma_j \xi)], \quad b_1 \leqslant \xi < r, \tag{51}$$

$$G_{mj}^{(B)}(r;\xi) = \frac{1}{\gamma_{mj} - \delta_{mj}}[\mathrm{I}_m(\sigma_j r) - \gamma_{mj}\mathrm{K}_m(\sigma_j r)] \cdot [\mathrm{I}_m(\sigma_j \xi) - \delta_{mj}\mathrm{K}_m(\sigma_j \xi)], \quad r < \xi \leqslant b, \tag{52}$$

where

$$\gamma_{mj} = \mathrm{I}'_m(\sigma_j b_1)/\mathrm{K}'_m(\sigma_j b_1) \text{ and } \delta_{mj} = \mathrm{I}'_m(\sigma_j b)/\mathrm{K}'_m(\sigma_j b). \tag{53a,b}$$

It is evident that the above form of Green's function satisfies also the property of symmetry $G_{mj}^{(B)}(r;\xi) = G_{mj}^{(B)}(\xi;r)$, as required.

By using Eqs. (34a), (34b), (36), (45) and (48), the 'trapped' wave component can be recast after extensive mathematical manipulations into

$$\varphi_{2B}^{DD}(r,\theta,z) = -\mathrm{i}\omega\left(\frac{H}{2}\right)^2 \sum_{m=-\infty}^{\infty} \mathrm{i}^m \Psi_m^{(2B,DD)}(r,z)\mathrm{e}^{\mathrm{i}m\theta}, \tag{54}$$

where

$$\Psi_m^{(2B,DD)}(r,z) = \frac{\kappa b_1}{\kappa h}\frac{\kappa b_1}{\kappa(h-h_1)}\sum_{j=0}^{\infty} Y_j^{(2)}(z)\,Y_j^{(2)}(h)\int_1^{b/b_1}\frac{\xi}{b_1}\,Q_m^{(B)}\left(\frac{\xi}{b_1}\right)G_{mj}^{(B)}\left(\frac{r}{b_1};\frac{\xi}{b_1}\right)\mathrm{d}\left(\frac{\xi}{b_1}\right). \tag{55}$$

2.3. Second-order 'free' wave potential φ_{2B}^{ID}

The form which was adopted for the 'trapped' wave component φ_{2B}^{DD} and was expressed through Eq. (54) will also be used in the following, for all second-order potentials in both fields $\boldsymbol{A}$ and $\boldsymbol{B}$. As far as the 'free' wave component φ_{2B}^{ID} is concerned, a general expression that satisfies the kinematical condition on the horizontal step Eq. (19a), the homogeneous free surface condition (21) and the Laplace Eq. (18a), will be given by an equation similar to (54), where $\Psi_m^{(2B,ID)}$ is expressed as

$$\Psi_m^{(2B,ID)}(r,z) = \sum_{j=0}^{\infty} F_{mj}^{(2B)} R_{mj}^{(2B)}(r)\,Y_j^{(2)}(z), \tag{56}$$

while $R_{mj}^{(2B)}(r)$ is described as indicated in Eqs. (25)–(27) provided that μ_j is replaced by σ_j.

A quick inspection of $R_{mj}^{(2B)}(r)$ verifies that the 'free' wave component $\Psi_m^{(2B,ID)}$ satisfies also the requirement for zero velocity on the wall, along the inner radius $r = b_1$.

2.4. Second-order diffraction potential for the outer field A

The outer fluid domain $\boldsymbol{A}$ is extended from $r = b$ to infinity. Thus, for the derivation of the corresponding diffraction potential, the equivalent bottom-seated cylinder with radius b can be considered. The problem of finding the second-order diffraction potential for a uniform bottom-seated, surface-piercing, vertical cylinder is well posed in the literature, as it has attracted the attention of several researchers in recent years, as discussed in the Introduction. Therefore, the part of the present paper which deals with that specific problem is inevitably short.

The total second-order velocity potential φ_{2A} for the outer wave field $\boldsymbol{A}$ should satisfy the Laplace equation and the following boundary conditions:

$$\left(\frac{\partial\varphi_{2A}}{\partial z}\right)_{z=0} = 0, \quad b \leqslant r, \tag{57}$$

$$\left(-4\nu\varphi_{2A} + \frac{\partial\varphi_{2A}}{\partial z}\right)_{z=h} = q_A(r,\theta), \quad b \leqslant r, \tag{58}$$

$$\left(\frac{\partial\varphi_{2A}}{\partial r}\right)_{r=b} = 0, \quad 0 \leqslant z \leqslant h_1. \tag{59}$$

For the complete description of the hydrodynamic problem in the outer field $\boldsymbol{A}$, Eqs. (57)–(59) should be supplemented by Eqs. (15) and (16) which express the continuity of velocities and potentials on the common boundary between fields $\boldsymbol{A}$ and $\boldsymbol{B}$.

In Eq. (58), $q_A(r,\theta)$ is the effective pressure distribution on the free surface of the outer field $\boldsymbol{A}$ and it is given by Eq. (8), provided that φ_1^D is replaced by the first-order diffraction potential φ_{1A}^D.

According to the majority of the proposed methods, the potential is decomposed into three components: the double frequency incident wave φ_2^I, the 'locked' wave φ_{2A}^{DD} and the 'free' wave φ_{2A}^{ID}. Thus,

$$\varphi_{2A} = \varphi_2^I + \varphi_{2A}^{ID} + \varphi_{2A}^{DD}. \tag{60}$$

All three component potentials should satisfy individually the Laplace equation. The second-order undisturbed incident wave potential φ_2^I is expressed by (Mei, 1983)

$$\varphi_2^I(r,\theta,z) = -\mathrm{i}\omega\left(\frac{H}{2}\right)^2 \sum_{m=-\infty}^{\infty} \mathrm{i}^m \Psi_m^I(r,z)\mathrm{e}^{\mathrm{i}m\theta}, \tag{61}$$

$$\Psi_m^I(r,z) = \frac{3}{8}\frac{\cosh(2\kappa z)}{\sinh^4(\kappa h)}\mathrm{J}_m(2\kappa r), \tag{62}$$

where J_m is the mth order Bessel function of the first kind. Furthermore, with regard to the 'locked' wave and the 'free' wave components, the boundary conditions which must be satisfied and which will allow later the matching of total potentials of fields $\boldsymbol{A}$ and $\boldsymbol{B}$, are

$$\left(\frac{\partial\varphi_{2A}^{ID}}{\partial z}\right)_{z=0} = 0, \quad \left(\frac{\partial\varphi_{2A}^{DD}}{\partial z}\right)_{z=0} = 0, \quad b \leqslant r, \tag{63a,b}$$

$$\left(-4\nu\varphi_{2A}^{ID} + \frac{\partial\varphi_{2A}^{ID}}{\partial z}\right)_{z=h} = 0, \quad b \leqslant r, \tag{64}$$

$$\left(-4\nu\varphi_{2A}^{DD} + \frac{\partial\varphi_{2A}^{DD}}{\partial z}\right)_{z=h} = q_A(r,\theta) - q_{II}, \quad b \leqslant r, \tag{65}$$

$$\left(\frac{\partial\varphi_{2A}^{DD}}{\partial r}\right)_{r=b} = 0, \quad 0 \leqslant z \leqslant h. \tag{66}$$

According to Eqs. (63b), (65) and (66), it is evident that the mathematical formulation which yields the 'locked' wave component is fully described. The latter implies that there is sufficient information for the calculation of φ_{2A}^{DD} which is obtained for the corresponding hypothetical, bottom-seated uniform cylinder, with radius b. On the contrary, the above equations do not anticipate the adoption of the 'free' wave potential φ_{2A}^{ID} on the boundary $r = b$ for $0 \leqslant z \leqslant h$. This will be accomplished in the following section by matching the total potentials φ_{2A} and φ_{2B} on the large radius b.

In accordance with the form adopted through Eqs. (54) and (61) for writing the second-order potentials, it can be shown that the 'locked' wave component $\Psi_m^{(2A,DD)}$ is given by (Huang and Eatock Taylor, 1996)

$$\Psi_m^{(2A,DD)}(r,z) = \sum_{j=0}^{\infty} Z_j^{(2)}(z)Z_j^{(2)}(h)\int_1^{\infty}\frac{\xi}{b}Q_m^{(A)}\left(\frac{\xi}{b}\right)G_{mj}^{(A)}\left(\frac{r}{b};\frac{\xi}{b}\right)\mathrm{d}\left(\frac{\xi}{b}\right), \tag{67}$$

where $Q_m^{(A)}$ is obtained by the pressure distribution for field $\boldsymbol{A}$ (Eqs. (8) and (65)). The functions $Q_m^{(A)}$ and $Q_m^{(B)}$ are very lengthy expressions and therefore their details are omitted. Furthermore, $Z_j^{(2)}(z)$ are orthonormal functions in $[0,h]$ given by

$$Z_0^{(2)}(z) = (N_0^{(2)})^{-1/2}\cosh(\rho_A z), \tag{68}$$

$$Z_j^{(2)}(z) = (N_j^{(2)})^{-1/2}\cos(k_j z), \quad j \geqslant 1, \tag{69}$$

$$N_0^{(2)} = \frac{1}{2}\left[1 + \frac{\sinh(2\rho_A h)}{2\rho_A h}\right], \tag{70}$$

$$N_j^{(2)} = \frac{1}{2}\left[1 + \frac{\sin(2k_j h)}{2k_j h}\right], \quad j \geqslant 1, \tag{71}$$

where k_j are the roots of the transcendental equation

$$4\nu + k_j \tan(k_j h) = 0, \tag{72}$$

which has an infinite number of real roots for $j \geqslant 1$ and one imaginary root $k_0 = -\mathrm{i}\rho_A$ which is determined by the second-order dispersion equation

$$\rho_A \tanh(\rho_A h) = 4\nu. \tag{73}$$

Table 1
Convergence of the total nondimensional second-order horizontal and vertical forces $f_{x_2}^{(2)}$ and $f_{z_2}^{(2)}$ (real, imag) acting on a bottom-seated surface-piercing compound cylinder ($h/b = 8$, $\kappa b = 0.5$, $b_1/b = 0.5$, $h_1/h = 0.5$)

Number of eigenmodes	$f_{x_2}^{(2)}$	$f_{z_2}^{(2)}$
$J = 30$	(0.2371, 0.3403)	(−0.0313, −0.0606)
$J = 50$	(0.2361, 0.3400)	(−0.0314, −0.0606)
$J = 80$	(0.2341, 0.3394)	(−0.0316, −0.0606)
$J = 100$	(0.2341, 0.3394)	(−0.0316, −0.0606)
$J = 120$	(0.2341, 0.3394)	(−0.0316, −0.0606)

Table 2
Convergence of the total nondimensional second-order horizontal and vertical forces $f_{x_2}^{(2)}$ and $f_{z_2}^{(2)}$ (real, imag) acting on a bottom-seated surface-piercing compound cylinder ($h/b = 8$, $\kappa b = 1.0$, $b_1/b = 0.5$, $h_1/h = 0.5$)

Number of eigenmodes	$f_{x_2}^{(2)}$	$f_{z_2}^{(2)}$
$J = 30$	(0.2468, 1.1916)	(−0.0298, −0.2282)
$J = 50$	(0.2466, 1.1907)	(−0.0298, −0.2287)
$J = 80$	(0.2465, 1.1896)	(−0.0299, −0.2290)
$J = 100$	(0.2465, 1.1896)	(−0.0298, −0.2289)
$J = 120$	(0.2465, 1.1896)	(−0.0297, −0.2289)

Table 3
Convergence of the total nondimensional second-order horizontal and vertical forces $f_{x_2}^{(2)}$ and $f_{z_2}^{(2)}$ (real, imag) acting on a bottom-seated surface-piercing compound cylinder ($h/b = 8$, $\kappa b = 2.0$, $b_1/b = 0.5$, $h_1/h = 0.5$)

Number of eigenmodes	$f_{x_2}^{(2)}$	$f_{z_2}^{(2)}$
$J = 30$	(0.9994, 1.7116)	(−0.0045, −0.3937)
$J = 50$	(0.9983, 1.7095)	(−0.0034, −0.3938)
$J = 80$	(0.9975, 1.7083)	(−0.0029, −0.3948)
$J = 100$	(0.9976, 1.7085)	(−0.0029, −0.3941)
$J = 120$	(0.9977, 1.7085)	(−0.0028, −0.3937)

Table 4
Convergence of the total nondimensional second-order horizontal and vertical forces $f_{x_2}^{(2)}$ and $f_{z_2}^{(2)}$ (real, imag) acting on a bottom-seated surface-piercing compound cylinder ($h/b = 10$, $\kappa b = 0.8$, $b_1/b = 0.5$, $h_1/h = 0.5$)

Number of eigenmodes	$f_{x_2}^{(2)}$	$f_{z_2}^{(2)}$
$J = 30$	(0.2924, 0.8565)	(−0.0221, −0.1237)
$J = 50$	(0.2921, 0.8559)	(−0.0223, −0.1241)
$J = 80$	(0.2918, 0.8551)	(−0.0224, −0.1241)
$J = 100$	(0.2918, 0.8552)	(−0.0224, −0.1243)
$J = 120$	(0.2918, 0.8552)	(−0.0224, −0.1243)

Finally, $G_{mj}^{(A)}$ is the one-dimensional Green's function

$$G_{mj}^{(A)}(r;\xi) = \mathrm{K}_m(k_j\xi)[\mathrm{I}_m(k_j r) - \mathrm{I}'_m(k_j b)\mathrm{K}_m(k_j r)/\mathrm{K}'_m(k_j b)], \quad r<\xi, \tag{74}$$

$$G_{mj}^{(A)}(r;\xi) = \mathrm{K}_m(k_j r)[\mathrm{I}_m(k_j\xi) - \mathrm{I}'_m(k_j b)\mathrm{K}_m(k_j\xi)/\mathrm{K}'_m(k_j b)], \quad r>\xi. \tag{75}$$

The 'free' wave component in $\boldsymbol{A}$ can be written in a form similar to the first-order diffraction potential of the outer field

$$\Psi_m^{(2A,ID)}(r,z) = \sum_{j=0}^{\infty} F_{mj}^{(2A)} \frac{\mathrm{K}_m(k_j r)}{\mathrm{K}_m(k_j b)} Z_j^{(2)}(z), \tag{76}$$

where $F_{mj}^{(2A)}$ are the unknown Fourier coefficients. The corresponding methodology which yields both series of Fourier coefficients $F_{mj}^{(2A)}$ and $F_{mj}^{(2B)}$ is outlined below.

2.5. Continuity of velocities and potentials at $r = b$

The expressions for $\Psi_m^{(2B,DD)}$, $\Psi_m^{(2B,ID)}$, Ψ_m^{I}, $\Psi_m^{(2A,DD)}$ and $\Psi_m^{(2A,ID)}$, are derived as solutions of the Laplace equation and are constructed in such a way that the boundary conditions on all horizontal boundaries of the fluid regions shown in Fig. 1 will be fulfilled. The last conditions that should be enforced are the continuity of radial velocities and potentials on the vertical boundary at $r = b$ for $h_1 \leqslant z \leqslant h$ (Eqs. (15) and (16)) and the zero velocity condition on the wall for $r = b$ $0 \leqslant z \leqslant h_1$ (Eq. (59). These will allow the calculation of Fourier coefficients $F_{mj}^{(2A)}$ and $F_{mj}^{(2B)}$. Thus,

$$\underbrace{\left.\frac{\partial\Psi_m^{(2A,DD)}}{\partial r}\right|_{r=b}}_{=0} + \left.\frac{\partial\Psi_m^{(2A,ID)}}{\partial r}\right|_{r=b} + \left.\frac{\partial\Psi_m^{I}}{\partial r}\right|_{r=b} = \underbrace{\left.\frac{\partial\Psi_m^{(2B,DD)}}{\partial r}\right|_{r=b}}_{=0} + \left.\frac{\partial\Psi_m^{(2B,ID)}}{\partial r}\right|_{r=b}, \quad h_1 \leqslant z \leqslant h, \tag{77}$$

$$\Psi_m^{(2A,DD)}\big|_{r=b} + \Psi_m^{(2A,ID)}\big|_{r=b} + \Psi_m^{I}\big|_{r=b} = \Psi_m^{(2B,DD)}\big|_{r=b} + \Psi_m^{(2B,ID)}\big|_{r=b}, \quad h_1 \leqslant z \leqslant h, \tag{78}$$

Table 5
Convergence of the total nondimensional second-order horizontal and vertical forces $f_{x_2}^{(2)}$ and $f_{z_2}^{(2)}$ (real, imag) acting on a bottom-seated surface-piercing compound cylinder ($h/b = 15$, $\kappa b = 0.8$, $b_1/b = 0.5$, $h_1/h = 0.5$)

Number of eigenmodes	$f_{x_2}^{(2)}$	$f_{z_2}^{(2)}$
$J = 30$	(0.4754, 0.6847)	(−0.0077, −0.0809)
$J = 50$	(0.4753, 0.6844)	(−0.0080, −0.0816)
$J = 80$	(0.4752, 0.6840)	(−0.0083, −0.0821)
$J = 100$	(0.4752, 0.6840)	(−0.0082, −0.0820)
$J = 120$	(0.4752, 0.6841)	(−0.0081, −0.0819)

Table 6
Convergence of the total nondimensional second-order horizontal and vertical forces $f_{x_2}^{(2)}$ and $f_{z_2}^{(2)}$ (real, imag) acting on a bottom-seated surface-piercing compound cylinder ($h/b = 25$, $\kappa b = 0.8$, $b_1/b = 0.5$, $h_1/h = 0.5$)

Number of eigenmodes	$f_{x_2}^{(2)}$	$f_{z_2}^{(2)}$
$J = 30$	(0.2499, 0.8300)	(−0.0012, −0.0467)
$J = 50$	(0.2499, 0.8317)	(−0.0017, −0.0477)
$J = 80$	(0.2499, 0.8312)	(−0.0024, −0.0487)
$J = 100$	(0.2499, 0.8314)	(−0.0021, −0.0485)
$J = 120$	(0.2499, 0.8315)	(−0.0020, −0.0484)

$$\underbrace{\left.\frac{\partial \Psi_m^{(2A,DD)}}{\partial r}\right|_{r=b}}_{=0} + \left.\frac{\partial \Psi_m^{(2A,ID)}}{\partial r}\right|_{r=b} + \left.\frac{\partial \Psi_m^{I}}{\partial r}\right|_{r=b} = 0, \quad 0 \leqslant z \leqslant h_1. \tag{79}$$

It is recalled that $Z_j^{(2)}(z)$ and $Y_j^{(2)}(z)$ are orthonormal functions in $[0,h]$ and $[h_1,h]$, respectively. In order to use the property of orthogonality which is satisfied by $Y_j^{(2)}(z)$ eigenfunctions, all terms in Eq. (78) are multiplied with an arbitrary $Y_p^{(2)}(z)$ and the resulting products are integrated over $[h_1,h]$. The implementation of the orthogonality relation will transform Eq. (78) to an appropriate expression which will provide the Fourier coefficients $F_{mj}^{(2B)}$ in terms of the corresponding elements $F_{mj}^{(2A)}$ of the 'free' wave potential $\Psi_m^{(2A,ID)}$:

$$\begin{aligned} F_{mj}^{(2B)} = & -Y_j^{(2)}(h)\frac{\kappa b_1}{\kappa h}\frac{\kappa b_1}{\kappa(h-h_1)}\int_1^{b/b_1}\frac{\xi}{b_1}Q_m^{(B)}\left(\frac{\xi}{b_1}\right)G_{mj}^{(B)}\left(\frac{b}{b_1};\frac{\xi}{b_1}\right)\mathrm{d}\left(\frac{\xi}{b_1}\right)+\frac{3}{8}\frac{\mathrm{J}_m(2\kappa b)}{\sinh^4(\kappa h)}P_j \\ & +\sum_{p=0}^{\infty}F_{mp}^{(2A)}V_{jp}^{(2)}+\sum_{p=0}^{\infty}Z_p^{(2)}(h)V_{jp}^{(2)}\int_1^{\infty}\frac{\xi}{b}Q_m^{(A)}\left(\frac{\xi}{b}\right)G_{mp}^{(A)}\left(1;\frac{\xi}{b}\right)\mathrm{d}\left(\frac{\xi}{b}\right). \end{aligned} \tag{80}$$

Using a similar procedure, all terms in Eqs. (77) and (79) are multiplied by an arbitrary $Z_l^{(2)}(z)$ and subsequently the resulting equations are integrated over $[h_1,h]$ and $[0,h_1]$, respectively. The summation of the corresponding equations will include integrals in which the orthogonality of $Z_j^{(2)}(z)$ eigenfunctions can be directly applied and the following relation is derived:

$$(k_l h)F_{ml}^{(2A)}\frac{\mathrm{K}'_m(k_l b)}{\mathrm{K}_m(k_l b)} = -\frac{3}{4}\frac{\mathrm{J}'_m(2\kappa b)}{\sinh^4(\kappa h)}(\kappa h)W_l + \sum_{j=0}^{\infty}F_{mj}^{(2B)}\sigma_j(h-h_1)R'^{(2B)}_{mj}(\sigma_j b)V_{jl}^{(2)}. \tag{81}$$

Combining Eqs. (80) and (81), the Fourier coefficients $F_{mj}^{(2A)}$ will be given by the following truncated linear matrix system:

$$[E_{pp}]_m\{F_{mp}^{(2A)}\} = \{D_p\}_m, \tag{82}$$

Table 7
Convergence of the total nondimensional second-order horizontal and vertical forces $f_{x_2}^{(2)}$ and $f_{z_2}^{(2)}$ (real, imag) acting on a bottom-seated surface-piercing compound cylinder ($h/b = 4$, $\kappa b = 1.0$, $b_1/b = 0.5$, $h_1/h = 0.5$)

Number of eigenmodes	$f_{x_2}^{(2)}$	$f_{z_2}^{(2)}$
$J = 30$	(0.2817, 1.2513)	(−0.1475, −0.4558)
$J = 50$	(0.2812, 1.2476)	(−0.1475, −0.4559)
$J = 80$	(0.2812, 1.2387)	(−0.1478, −0.4557)
$J = 100$	(0.2813, 1.2388)	(−0.1478, −0.4556)
$J = 120$	(0.2813, 1.2389)	(−0.1478, −0.4556)

Table 8
Convergence of the total nondimensional second-order horizontal and vertical forces $f_{x_2}^{(2)}$ and $f_{z_2}^{(2)}$ (real, imag) acting on a bottom-seated surface-piercing compound cylinder ($h/b = 2$, $\kappa b = 2.0$, $b_1/b = 0.5$, $h_1/h = 0.5$)

Number of eigenmodes	$f_{x_2}^{(2)}$	$f_{z_2}^{(2)}$
$J = 30$	(0.9803, 1.8813)	(0.0346, −1.5338)
$J = 50$	(0.9810, 1.8802)	(0.0352, −1.5326)
$J = 80$	(0.9852, 1.8793)	(0.0360, −1.5304)
$J = 100$	(0.9850, 1.8794)	(0.0360, −1.5303)
$J = 120$	(0.9850, 1.8794)	(0.0360, −1.5302)

which is solved m times for all p Fourier coefficients $F_{mp}^{(2A)}$. $[E_{pp}]$ is a square $(p \times p)$ complex matrix while $\{D_p\}$ is a $(p \times 1)$ column matrix. The elements of these matrices and the nondimensional factors W_l, $V_{jl}^{(2)}$ and P_j involved in Eqs. (80) and (81) are given in Appendix A. Finally, the corresponding Fourier coefficients for the upper inner fluid domain $\boldsymbol{B}$ can easily be determined through Eq. (80).

3. Numerical calculation and convergence of integrals

The solution method which is followed in the present work for the derivation of the second-order diffraction potentials is a semi-analytical formulation which allows matching of the potentials along the adjacent boundaries of the wave fields $\boldsymbol{A}$ and $\boldsymbol{B}$. The numerical part of the solution concerns only the calculation of integrals

$$I_{mj}^{(A)}(r) = \int_1^{\infty} \frac{\xi}{b} Q_m^{(A)}\left(\frac{\xi}{b}\right) G_{mj}^{(A)}\left(\frac{r}{b};\frac{\xi}{b}\right) \mathrm{d}\left(\frac{\xi}{b}\right), \tag{83}$$

$$I_{mj}^{(B)}(r) = \int_1^{b/b_1} \frac{\xi}{b_1} Q_m^{(B)}\left(\frac{\xi}{b_1}\right) G_{mj}^{(B)}\left(\frac{r}{b_1};\frac{\xi}{b_1}\right) \mathrm{d}\left(\frac{\xi}{b_1}\right) \tag{84}$$

at any point r of the wave fields $\boldsymbol{A}$ and $\boldsymbol{B}$. The numerical integration method which is implemented herein is a Gauss–Legendre N-point quadrature formula (Press et al., 1986). The analytical derivation of integrals is avoided because of the excessively complicated forms of the pressure distributions $Q_m^{(A)}$ and $Q_m^{(B)}$. The second integral (84) can be obtained easily as the integration limits are finite and, even for a large upper limit b/b_1, a small number of integration points provide satisfactory predictions. In all cases examined here, the use of 100 integration points was proven to be sufficient. The major difficulty arises from the first integral (83). Based on the fact that this expression

Table 9
Comparative results for nondimensional horizontal forces, acting on a bottom-seated surface-piercing uniform cylinder with $h = b$

νb		1.2		2.0		2.8	
		$\mathscr{R}e$	$\mathscr{I}m$	$\mathscr{R}e$	$\mathscr{I}m$	$\mathscr{R}e$	$\mathscr{I}m$
$f_x^{(1)}$	Kim and Yue (1989)	0.708	−2.351	−0.264	−1.606	−0.746	−0.743
	Present	0.712	−2.530	−0.259	−1.607	−0.742	−0.745
$f_{x_1}^{(2)}$	Kim and Yue (1989)	−1.648	−0.308	−1.094	0.849	0.892	1.341
	Present	−1.650	−0.312	−1.102	0.843	0.884	1.352
$f_{x_2}^{(2)}$	Kim and Yue (1989)	2.259	−0.136	1.972	−1.835	−2.209	−3.606
	Present	2.286	−0.143	1.988	−1.858	−2.218	−3.617

Table 10
Comparative results for the amplitudes of nondimensional horizontal forces acting on a bottom-seated surface-piercing uniform cylinder with $h/b = 4$

κb	$\lvert f_{x_2}^{(2)}\rvert$		$\lvert f_{x_1}^{(2)}\rvert$	
	Present	Mavrakos and Peponis (1992)	Present	Mavrakos and Peponis (1992)
1.0	3.020	3.000	1.412	1.492
1.2	3.735	3.717	1.666	1.641
1.4	4.400	4.473	1.868	1.868
1.6	4.965	4.968	1.987	1.958
1.8	5.123	5.089	1.821	1.821
2.0	4.935	5.033	1.516	1.545

is slowly convergent, a suitable manner to approach the integration is to split the integral. Thus, Eq. (83) can be transformed into

$$\int_1^{\infty} = \int_1^{r_1/b} + \int_{r_1/b}^{r_2/b} + \cdots + \int_{r_{n-1}/b}^{r_n/b} + \cdots. \tag{85}$$

The Gauss–Legendre quadrature formula is applied to all parts of the above summation. The necessary number of integration points in each integral depends on the distance between the integration limits. The larger the distance is, the more integration points are needed. In order to simplify the solution algorithm, evenly spaced limits have been selected. In particular, for all cases considered here, a difference of $100b$ was chosen, i.e., $r_n/b - r_{n-1}/b = 100$. Next, for the correct numerical prediction of each consecutive integral, a sufficient number of integration points must be used.

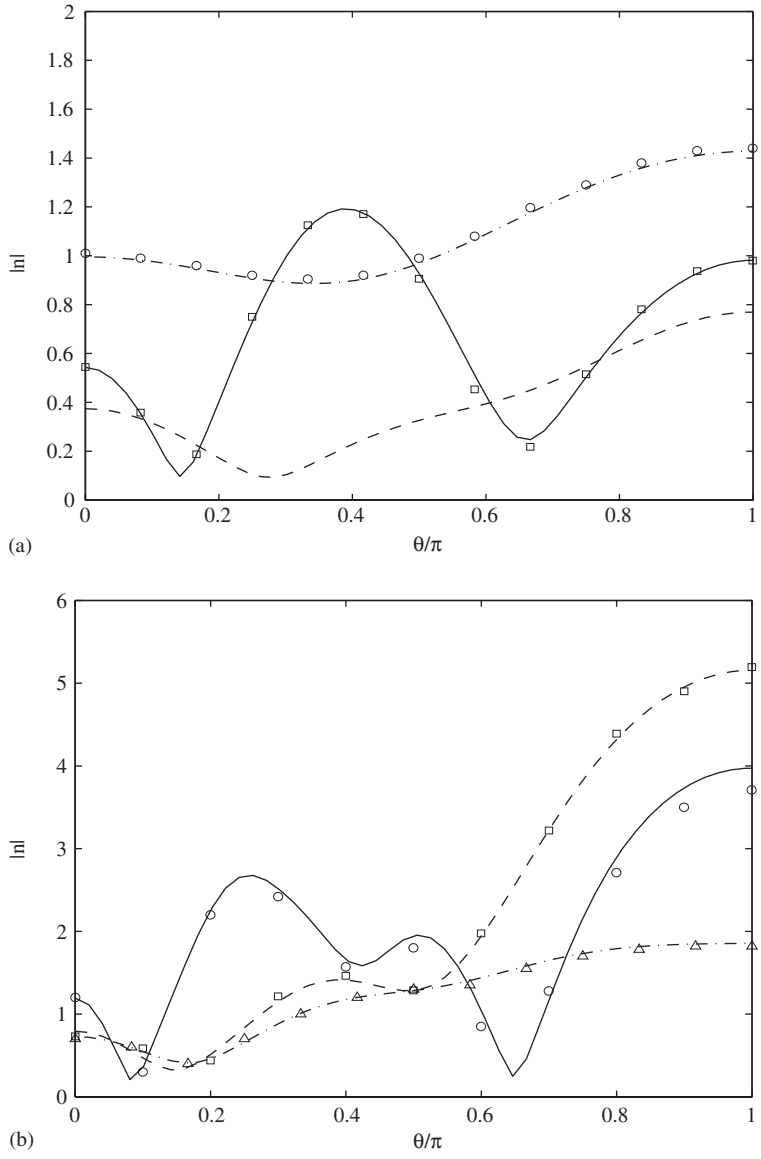

Fig. 2. Absolute values of dimensionless wave elevation around the circumference of a uniform, bottom-seated, surface-piercing, vertical cylinder: — · — · —, $|\eta^{(1)}/(H/2)|$; -------, $|\eta_1^{(2)}b/(H/2)^2|$; ———, $|\eta_2^{(2)}b/(H/2)^2|$. (a) $h/b = 8$, $vh = 4.024$, symbols denote results reported by Chau and Eatock Taylor (1992); (b) $h = b$, $vh = 2$, symbols denote results reported by Kim and Yue (1989).

A common rule for having an indication for the number of points which are needed in order to obtain satisfactory results is based on the fact that more points should be used for stronger anticipated diffraction phenomena (large b/h). Since the magnitude of the contribution of each integral to the total value is reduced for increasing n, the number of integration points which must be chosen can be controlled by inspecting the values of the first integral. The evaluation procedure is terminated when the value of an integral is smaller than a prescribed error or when the difference between two consecutive integrals is sufficiently small. The error values which were used in the present were 1×10^{-4} and 1×10^{-6}, respectively. This holds for all m, j and r.

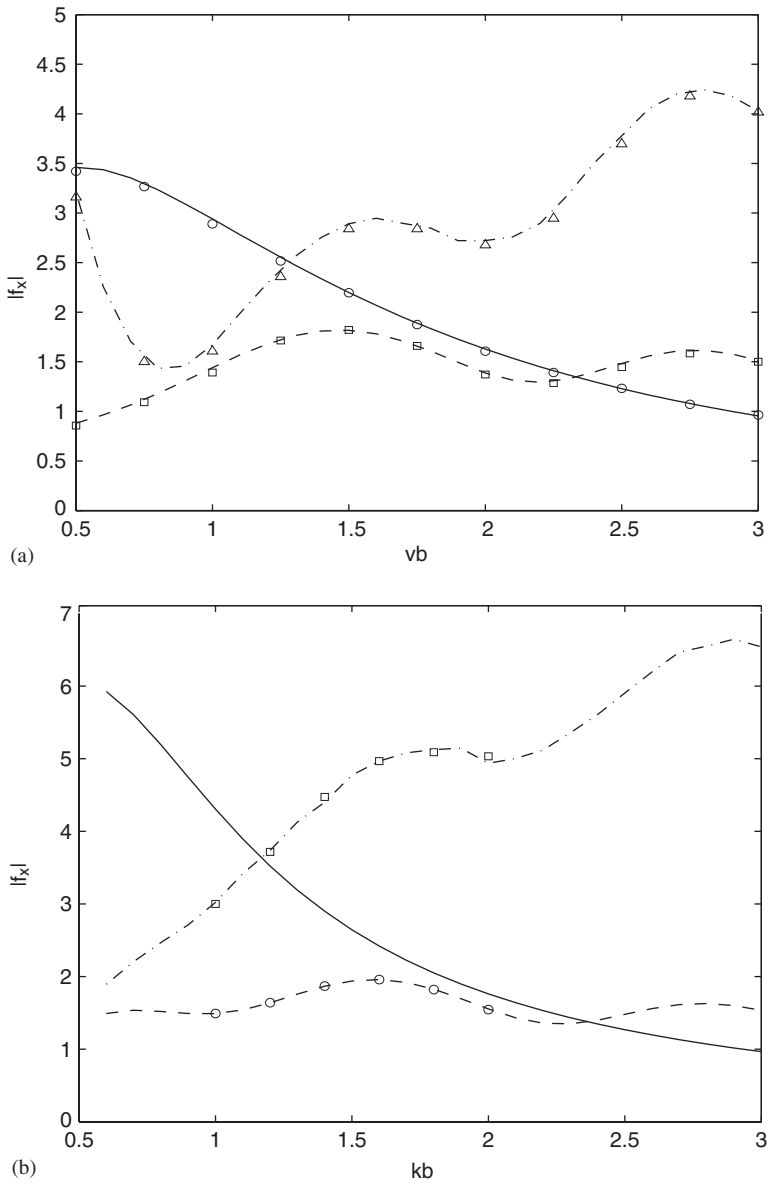

Fig. 3. Amplitudes of the first- and second-order wave excitation components in the horizontal direction on a uniform, bottom-seated, surface-piercing, vertical cylinder: ———, $|f_x^{(1)}|$; - - - - - - - - -, $|f_{x1}^{(2)}|$; — · — · —, $|f_{x2}^{(2)}|$; (a) $h = b$, symbols denote the results reported by Kim and Yue (1989), (b) $h = 4b$, symbols denote the results reported by Mavrakos and Peponis (1992).

4. Second-order wave elevation and wave loads

The final relations that describe the first- and second-order wave elevations and wave loads are very lengthy expressions. Therefore, only the general expressions are provided herein. However, it is important to notice that the integrals involved in the calculation of the vertical wave forces (integration with respect to the radial coordinate r) are determined numerically using the above-mentioned Gauss–Legendre quadrature formula.

The fluid force exerted on the body is obtained by integrating the fluid pressure over the submerged body surface. After omitting 3rd order terms and above, the following expressions for the time-varying first- and second-order forces

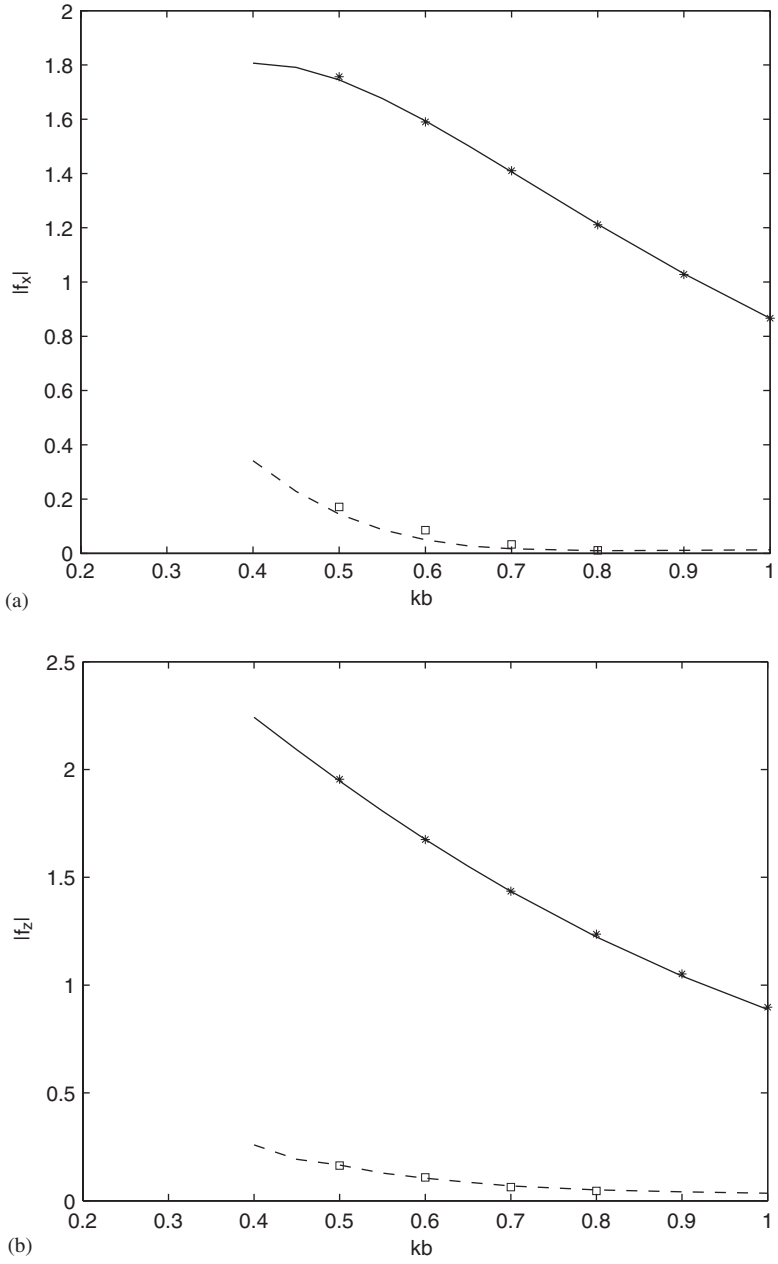

Fig. 4. Amplitudes of the first- and the second-order wave excitation components in the horizontal and vertical direction on a bottom-seated, submerged cylinder ($h/b = 3$, $h_1/h = 0.5$, $b_1/b = 0.01$): ———, $|f_x^{(1)}|$ and $|f_z^{(1)}|$; - - - - - - - - -, $|f_{x2}^{(2)}|$ and $|f_{z2}^{(2)}|$. Symbols denote the results reported by Abul-Azm and Williams (1988): (a) horizontal force, (b) vertical force.

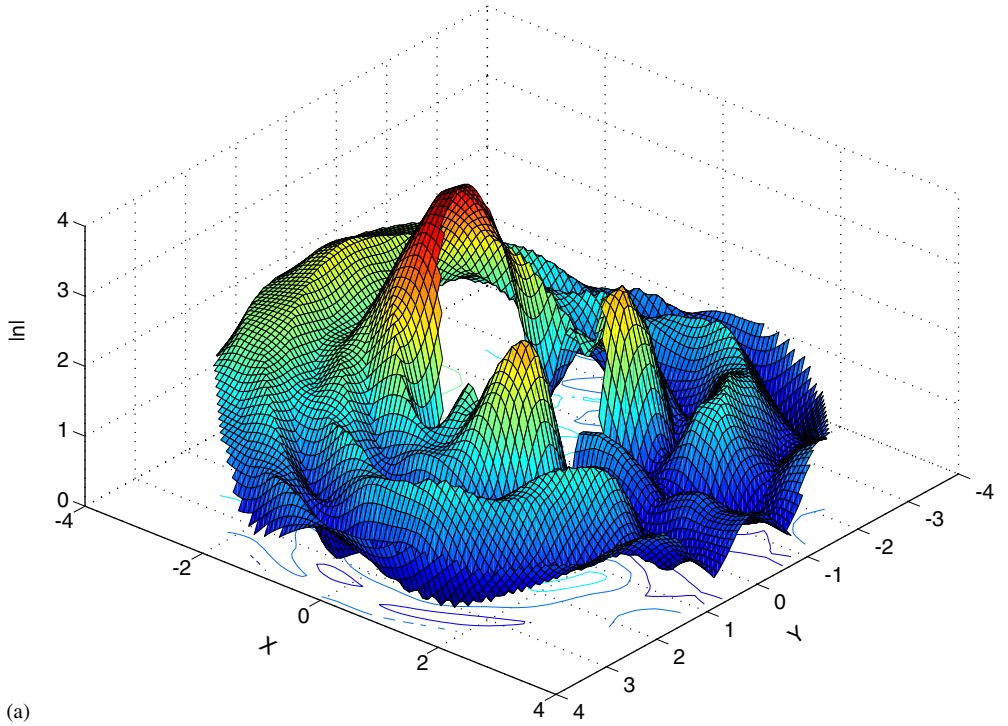

(a)

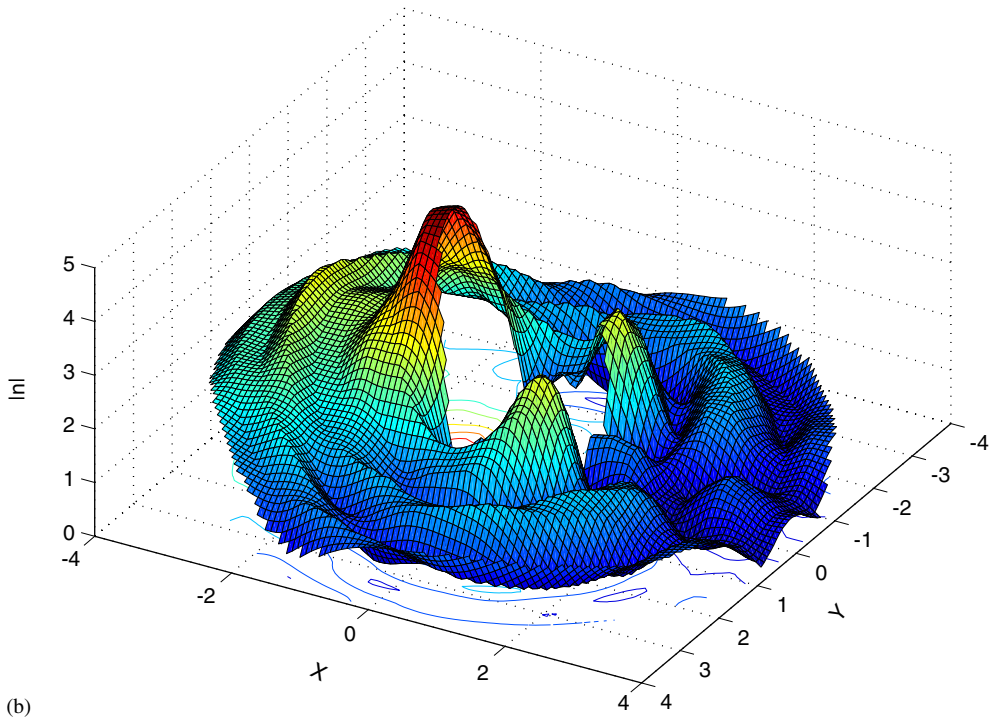

(b)

Fig. 5. Absolute values of dimensionless wave elevation $|\eta_2^{(2)}b/(H/2)^2|$ around a uniform, bottom-seated, surface-piercing vertical cylinder. (a) $\nu h = 2.0$, $\kappa b = 2.0653$, $h = b$, (b) $\nu h = 8.0$, $\kappa b = 2.0$, $h/b = 4$. Wave direction is from positive to negative X.

can be derived (Ogilvie, 1983):

$$F_k^{(1)} = \iint_{S_{B_0}} \mathrm{i}\omega\rho\varphi_1 n_k \,\mathrm{d}S, \tag{86}$$

$$F_k^{(2)} = \iint_{S_{B_0}} \left(2\mathrm{i}\omega\rho\varphi_2 - \frac{1}{4}\rho\nabla\varphi_1\nabla\varphi_1\right) n_k \,\mathrm{d}S + \frac{1}{4}\int_{C_{B_0}} \eta^{(1)}\eta^{(1)} n_k \,\mathrm{d}C, \tag{87}$$

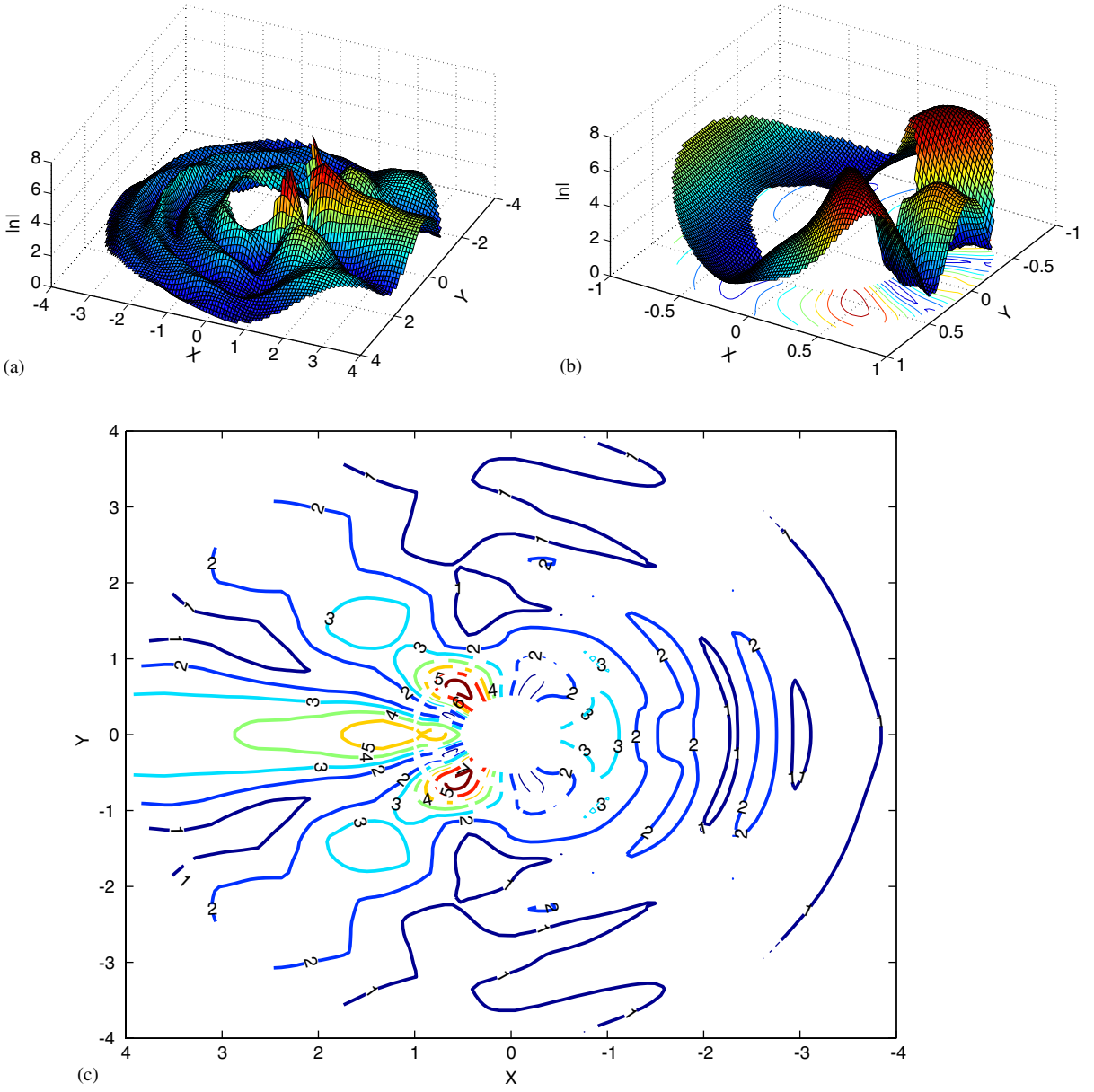

Fig. 6. Absolute values of dimensionless wave elevation $|\eta_2^{(2)}b/(H/2)^2|$ around a bottom-seated, surface-piercing, vertical compound cylinder for $\nu h = 2.0$, $\kappa b = 2.0653$, $h = b$, $h_1/h = 0.5$, $b_1/b = 0.5$: (a) outer field ***A***, (b) inner field ***B***, (c) contours of wave elevation in fields ***A*** and ***B***. Wave direction in contour is from left to right. Wave direction in 3-D plots is from positive to negative X.

where S_{B_0} is the mean wetted surface of the body, C_{B_0} is the waterline and n_k is the kth component of the normal which was chosen to point out of the fluid domain. Also, in the above equations, $\eta^{(1)}$ is the first-order wave elevation which is calculated by

$$\eta^{(1)} = \frac{\mathrm{i}\omega}{g}\varphi_1. \tag{88}$$

The corresponding second-order wave elevation—which also provides the wave run-up on the body for $r = b_1$ for a vertical compound cylinder—is given by

$$\eta^{(2)} = \frac{2\mathrm{i}\omega}{g}\varphi_2 - \frac{1}{4g}\nabla\varphi_1\nabla\varphi_1 - \frac{v^2}{2g}\varphi_1\varphi_1. \tag{89}$$

The numerical predictions for the wave elevation and wave loads which are presented in the following section have been normalized by $\rho g b^2(H/2)$ and $\rho g b(H/2)^2$ for the first- and second-order forces and by $H/2$ and $(H/2)^2/b$ for the

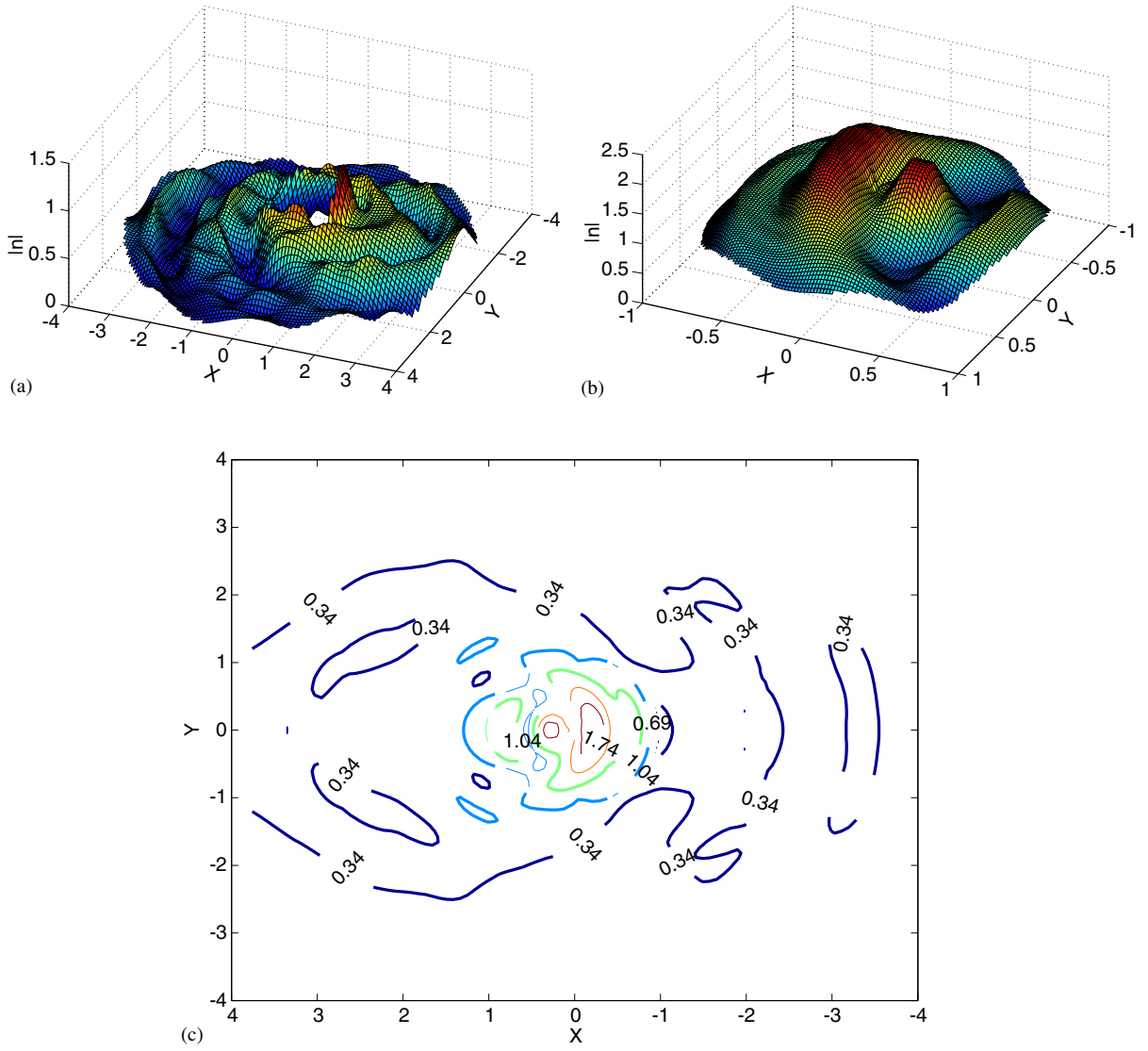

Fig. 7. Absolute values of dimensionless wave elevation $|\eta_2^{(2)}b/(H/2)^2|$ above a bottom-seated, fully submerged, vertical cylinder for $vh = 2.0$, $\kappa b = 2.0653$, $h = b$, $h_1/h = 0.5$, $b_1/b = 0.01$: (a) outer field $\boldsymbol{A}$, (b) inner field $\boldsymbol{B}$, (c) contours of wave elevation in fields $\boldsymbol{A}$ and $\boldsymbol{B}$. Wave direction in contour is from left to right. Wave direction in 3-D plots is from positive to negative X.

first- and second-order wave elevation, respectively. Finally, $\eta_1^{(2)}$, $F_{k_1}^{(2)}$ and $\eta_2^{(2)}$, $F_{k_2}^{(2)}$ will symbolize the components of the nonlinear wave elevation and wave forces which are obtained through the first- and second-order potentials, respectively.

5. Numerical results and discussion

The main objective of the present contribution is to introduce an efficient method for the solution of the second-order diffraction problem around a complex, one-step, bottom-seated, surface-piercing vertical cylinder and to investigate the changes in the water field with respect to the size of the small radius b_1 and the height of the step h_1. This is accomplished with the aid of the numerical predictions for the vertical and the horizontal second-order forces acting on

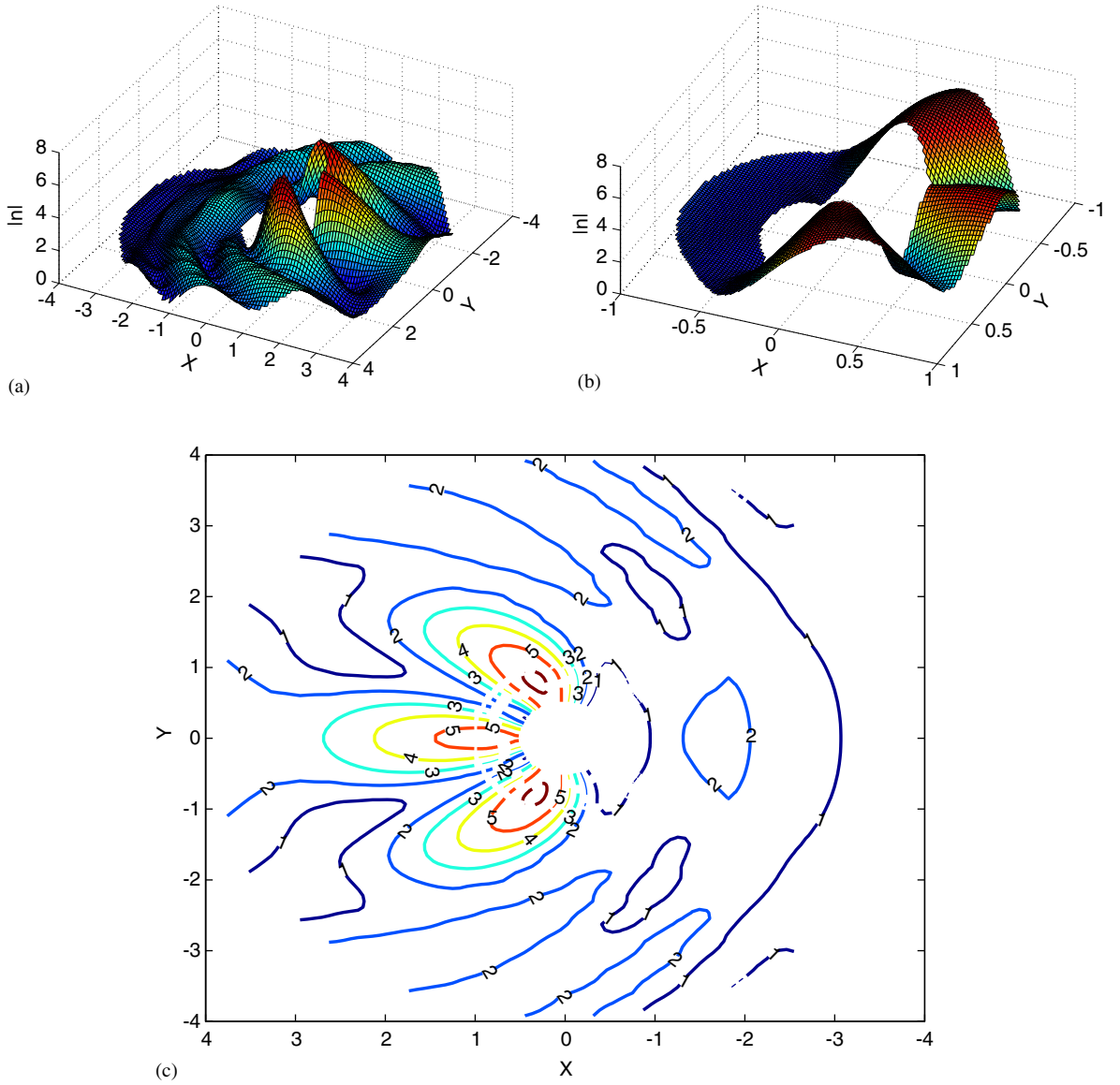

Fig. 8. Absolute values of dimensionless wave elevation $|\eta_2^{(2)}b/(H/2)^2|$ around a bottom-seated, surface-piercing, vertical compound cylinder for $\nu h = 1.0$, $\kappa b = 1.199$, $h = b$, $h_1/h = 0.5$, $b_1/b = 0.5$: (a) outer field ***A***, (b) inner field ***B***, (c) contours of wave elevation in fields ***A*** and ***B***. Wave direction in contour is from left to right. Wave direction in 3-D plots is from positive to negative X.

the cylinder and the wave elevation up to a sufficient radial distance from the body's wetted surface. The method outlined previously is appropriate to be used also for a uniform surface-piercing cylinder, as well as for a bottom-seated fully submerged cylinder. This can be carried out by adjusting the values of b_1 and h_1, which can vary in the ranges $[0,b]$ and $[0,h]$, respectively. These values can never coincide with the end-most limits of the afore-mentioned ranges as the method collapses. It is evident that this is actually an approximation but, as shown later, a very accurate one. In the present contribution, a uniform bottom-seated, surface-piercing cylinder is simulated by $h_1/h = 0.9$ and $b_1/b = 0.999$, and a fully submerged bottom-seated cylinder by $b_1/b = 0.01$.

5.1. Validation and convergence of the method

The convergence of the results which are obtained by the solution of the second-order diffraction problem depends on the number of Fourier coefficients M and the number of eigenmodes J in fields $\boldsymbol{A}$ and $\boldsymbol{B}$. It should be noted that for

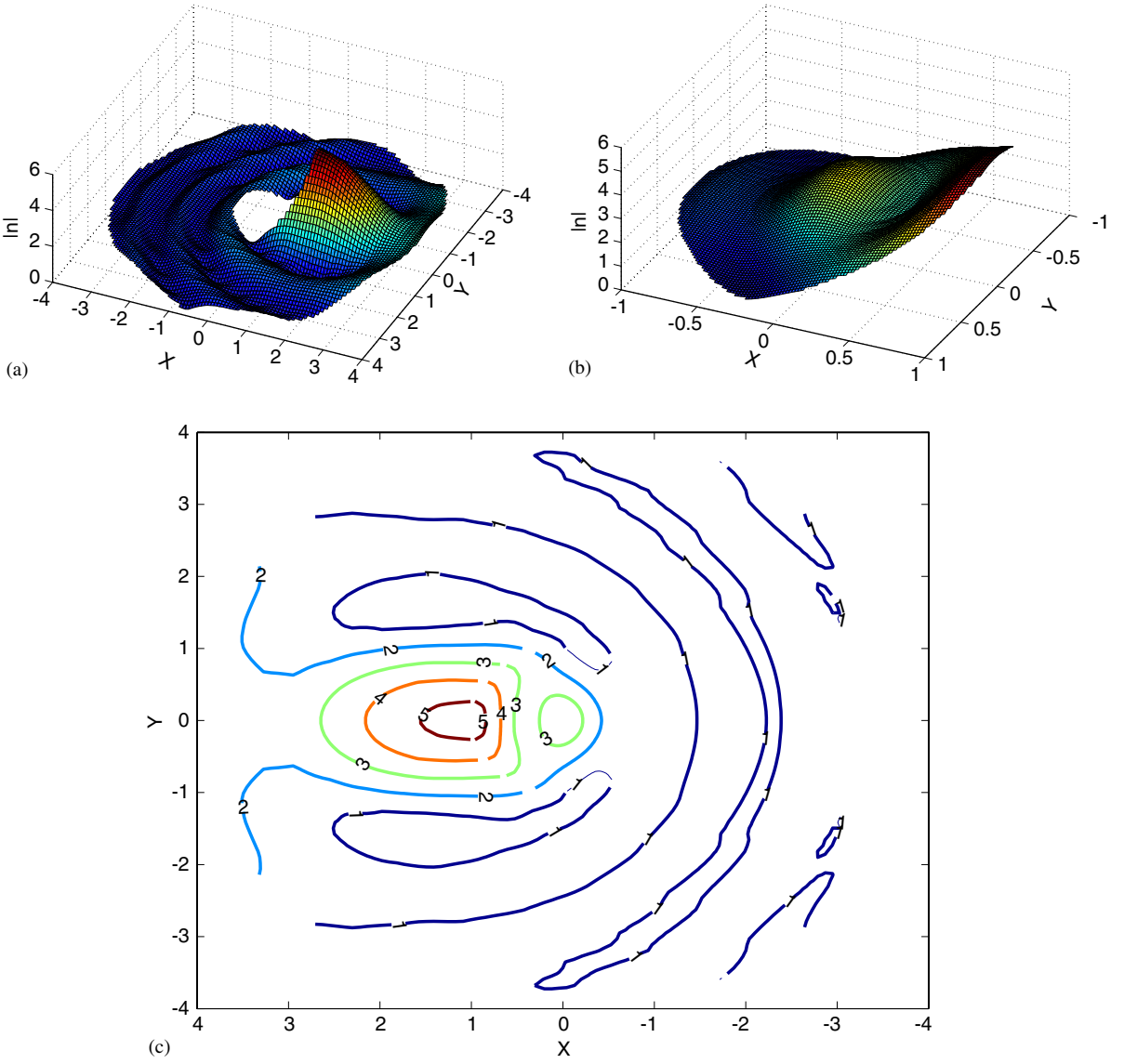

Fig. 9. Absolute values of dimensionless wave elevation $|\eta_2^{(2)}b/(H/2)^2|$ above a bottom-seated fully submerged, vertical cylinder for $vh = 1.0$, $\kappa b = 1.199$, $h = b$, $h_1/h = 0.5$, $b_1/b = 0.01$: (a) outer field $\boldsymbol{A}$, (b) inner field $\boldsymbol{B}$, (c) contours of wave elevation in fields $\boldsymbol{A}$ and $\boldsymbol{B}$. Wave direction in contour is from left to right. Wave direction in 3-D plots is from positive to negative X.

all calculations the number of eigenmodes in both fields was always equal, although the smaller height h–h_1 in the water region ***B*** could justify the use of fewer eigenmodes.

The use of a sufficiently large M for the Fourier coefficients which contribute to the solution will practically eliminate the dependence of the convergence from M. For all calculations performed for the purposes of the present contribution, M was set equal to 10, which was proven to be a satisfactory approximation. Thus, only the influence of vertical eigenmodes J is investigated here. The convergence of the results with respect to the number of the vertical eigenmodes J for various configurations of surface-piercing compound cylinders is examined with the aid of Tables 1–8. In all cylinders, the step on the body is located at the middle of the depth ($h_1/h = 0.5$) and the radius of the upper part of the body is equal to the half of the radius of the base ($b_1/b = 0.5$).

Tables 1–3 show the results for the nondimensional components of the second-order wave forces $f^{(2)}_{x_2}$ and $f^{(2)}_{z_2}$ which were obtained by convergence studies for constant κb and variable depth h/b, while Tables 4–6 show the corresponding results for constant water depth h/b and variable κb. In order to verify the conclusions regarding the number of eigenmodes that should be used for achieving acceptable convergence, additional runs were performed for various

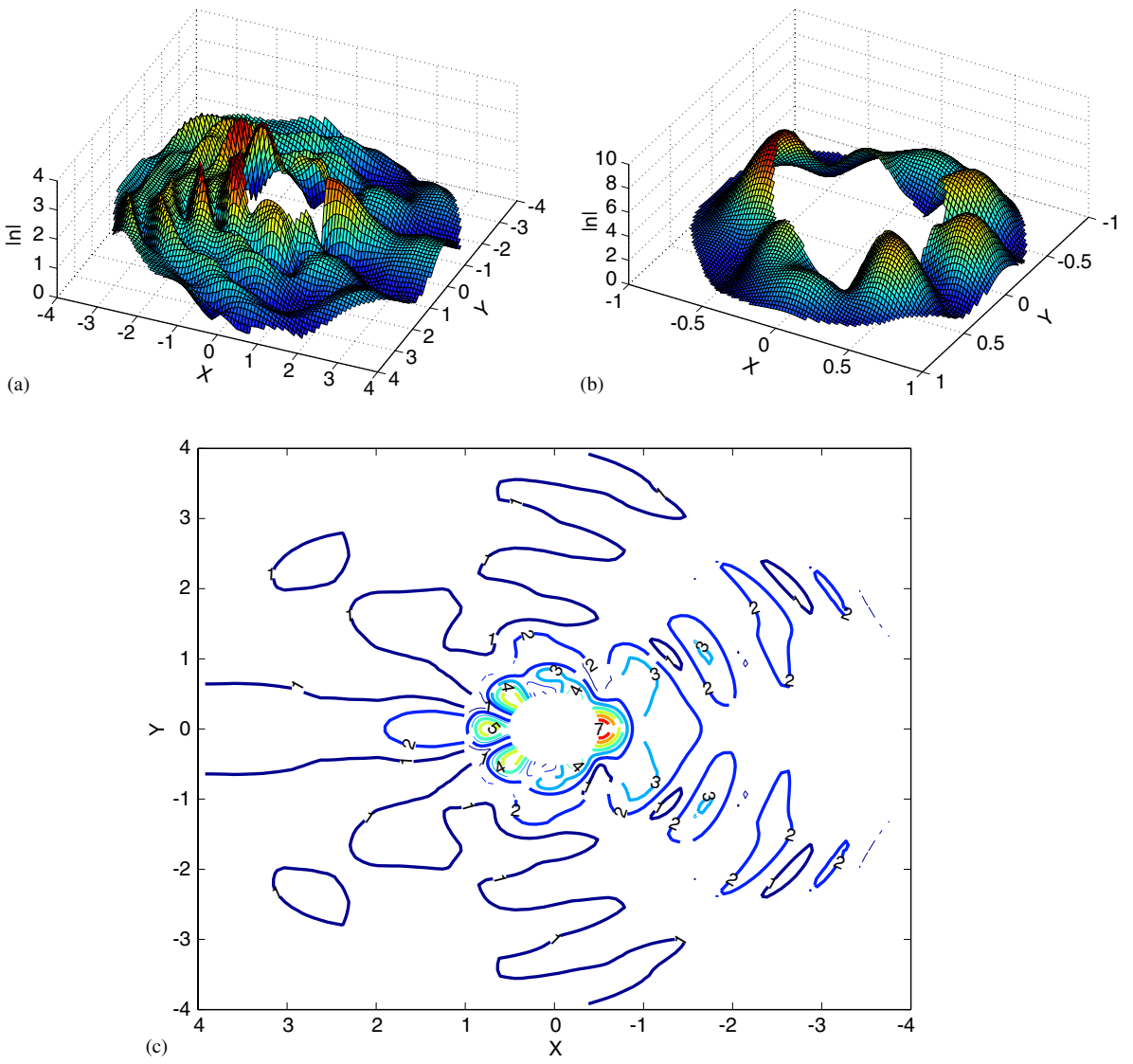

Fig. 10. Absolute values of dimensionless wave elevation $|\eta^{(2)}_2 b/(H/2)^2|$ around a bottom-seated, surface-piercing, vertical compound cylinder for $\nu h = 8.0$, $\kappa b = 2$, $h/b = 4$, $h_1/h = 0.2$, $b_1/b = 0.5$: (a) outer field ***A***, (b) inner field ***B***, (c) contours of wave elevation in fields A and B. Wave direction in contour is from left to right. Wave direction in 3-D plots is from positive to negative X.

cylinder types. Indicative results for different compound axisymmetric bodies are presented in Tables 7 and 8. By inspecting the values of forces that are listed in the tables, it is easy to conclude that the use of 10 Fourier coefficients and 50 vertical eigenmodes ensures an accuracy of more than 99%. This is valid even for very deep water (Table 6).

Next the efficacy of the present method is confirmed by comparing the calculated results with existing numerical data reported by other authors in the past. The comparisons concern uniform surface-piercing cylinders with $b \approx b_1$ and fully submerged cylinders with $b_1 \ll b$. To this end, Tables 9 and 10 and Figs. 2–4 are given. Table 9 shows the Real and Imaginary parts for the first- and the components of second-order exciting force on a uniform cylinder with $h = b$ and for three values of νb, while Table 10 lists the amplitudes of the second-order components on a cylinder with $h = 4b$ and for various κb. The same results are depicted also in Fig. 3. The comparison confirms the favourable coincidence between predictions by the present method and those due to Kim and Yue (1989) and Mavrakos and Peponis (1992), respectively.

Figs. 2(a) and (b) depict the wave run-up on two uniform bottom-seated, free-surface piercing cylinders with $h = 8b$ and $h = b$, respectively. A good agreement is again observed between the present results and those obtained by Chau and Eatock

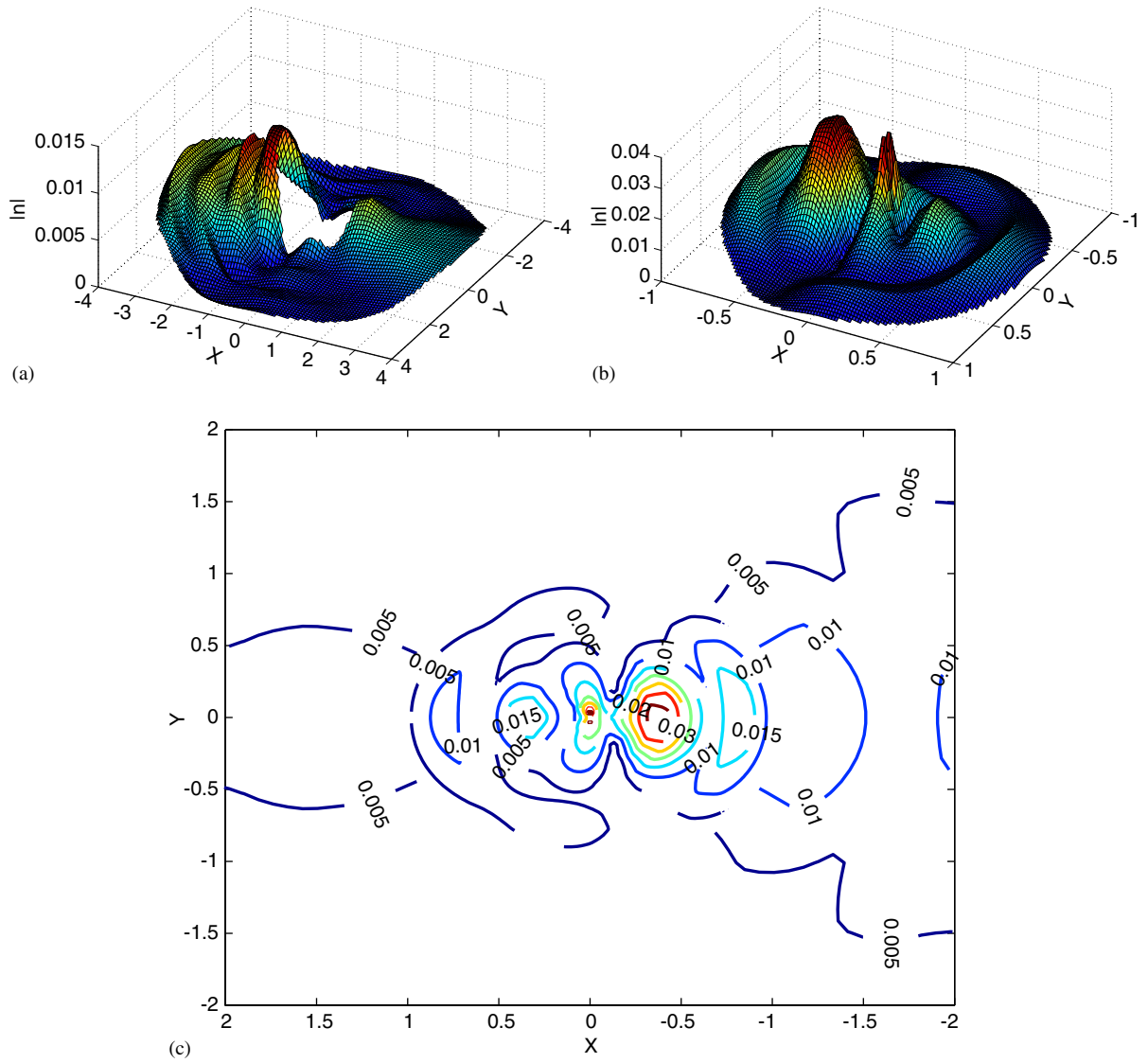

Fig. 11. Absolute values of dimensionless wave elevation $|\eta_2^{(2)}b/(H/2)^2|$ above a bottom-seated, fully submerged, vertical cylinder for $\nu h = 8.0$, $\kappa b = 2$, $h/b = 4$, $h_1/h = 0.2$, $b_1/b = 0.01$: (a) outer field $\boldsymbol{A}$, (b) inner field $\boldsymbol{B}$, (c) contours of wave elevation in fields $\boldsymbol{A}$ and $\boldsymbol{B}$. Wave direction in contour is from left to right. Wave direction in 3-D plots is from positive to negative X.

Taylor (1992) and Kim and Yue (1989). This demonstrates the effectiveness of the present method in providing reliable predictions, even if it is employed for studying the wave field around uniform cylinders. In particular, the results show a pronounced variation of wave run-up due to second-order potential in the whole range of azimuthal angle. The specific contribution is of the same order of magnitude when it is compared with the other second-order quantities for $h = b$, Fig. 2(b), and considerably higher for $h = 8b$, Fig. 2(a). As far as the wave loads are concerned, the contribution of the second-order potential is the major component of the total second-order terms. The corresponding horizontal nonlinear force exhibits a wavy trend, attaining higher values for larger κb or νb contrary to the first-order force which progressively decays (Fig. 3).

For confirming the effectiveness of the proposed semi-analytical solution methodology when it is used for solving the second-order diffraction problem around submerged cylindrical bodies, additional tests were performed for the calculation of the first- and second-order forces on a cylinder with $h/b = 3$, $h_1/h = 0.5$, $b_1/b = 0.01$. The results obtained by the present method, are compared in Fig. 4 with those reported by Abul-Azm and Williams (1988). As can be seen, the agreement is again quite satisfactory and it is observed that the contribution of the second-order effects is reduced as the wave frequency κb obtains higher values.

5.2. Wave elevation around a vertical one-step bottom-seated compound cylinder

This is investigated with the aid of Figs. 5–12. Fig. 5 shows the wave elevation around two different uniform cylinders. These plots are given as a reference for comparison with compound cylinders. In all 3-D plots, the Cartesian

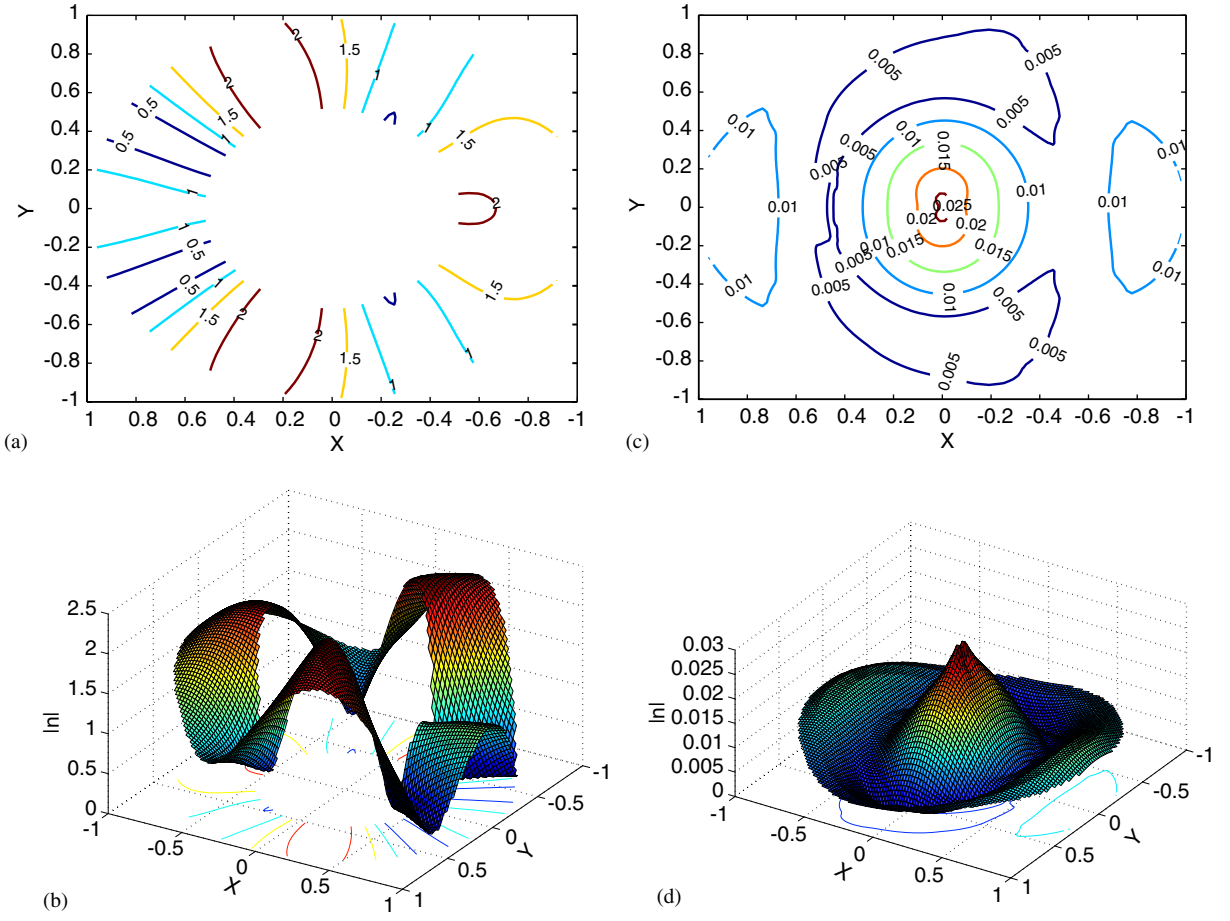

Fig. 12. Absolute values of dimensionless wave elevation $|\eta_2^{(2)}b/(H/2)^2|$ for a bottom-seated compound cylinder in the inner field $\boldsymbol{B}$ for $\nu h = 3.9973$, $\kappa b = 1.0$, $h/b = 4$, $h_1/h = 0.2$: (a)–(b) $b_1/b = 0.5$, (c)–(d) $b_1/b = 0.01$. Wave direction in contours is from left to right. Wave direction in 3-D plots is from positive to negative X.

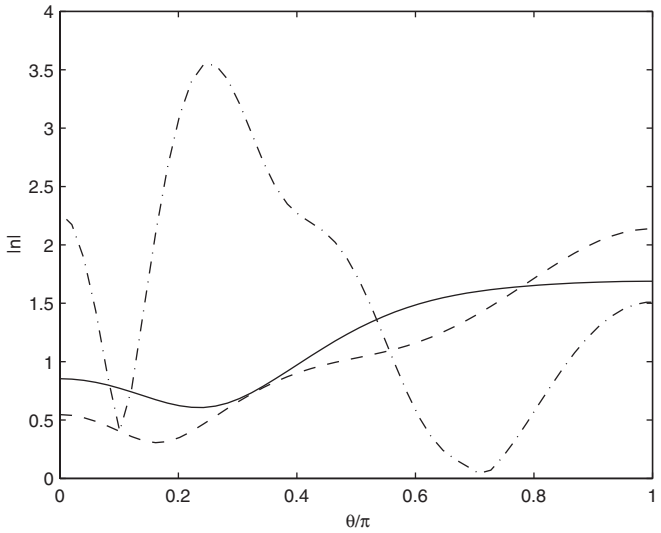

Fig. 13. Absolute values of dimensionless wave elevation around the circumference of a uniform bottom-seated, surface-piercing, vertical cylinder: ———, $|\eta^{(1)}/(H/2)|$; - - - - - - -, $|\eta_1^{(2)}b/(H/2)^2|$; — · — · —, $|\eta_2^{(2)}b/(H/2)^2|$; $\nu h = 1.0$, $\kappa b = 1.199$, $h = b$.

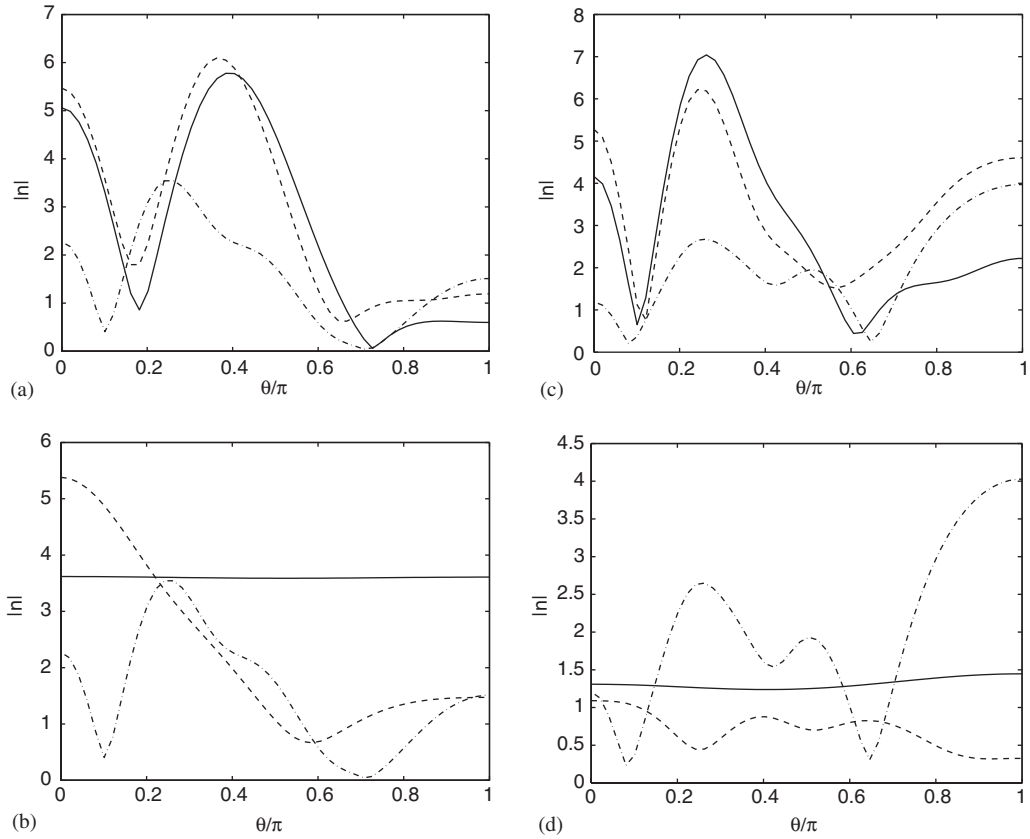

Fig. 14. Absolute values of dimensionless wave elevation $|\eta_2^{(2)}b/(H/2)^2|$, around a bottom-seated, surface-piercing, vertical compound cylinder: ———, run-up at $r = b_1$; - - - - - - - - -, wave elevation at $r = b$; — · — · —, run-up on the equivalent uniform, bottom- seated, surface-piercing vertical cylinder with uniform radius b. (a) $\nu h = 1.0$, $h = b$, $h_1/h = 0.5$, $b_1/b = 0.5$, (b) $\nu h = 1.0$, $h = b$, $h_1/h = 0.5$, $b_1/b = 0.01$, (c) $\nu h = 2.0$, $h = b$, $h_1/h = 0.5$, $b_1/b = 0.5$, (d) $\nu h = 2.0$, $h = b$, $h_1/h = 0.5$, $b_1/b = 0.01$.

coordinates have been normalized with respect to the large radius b. In these particular cases the wave elevation patterns due to the second-order potentials, appear to be similar, while for deeper water, Fig. 5(b), the maximum wave elevation is higher. In both cases the maximum run-up is detected on the lee side of the cylinder. The alteration in the wave field characteristics—and in general in the wave elevation—due to the change in cylinder's diameter is considered through 3-D plots in Figs. 6–9. These figures depict the wave elevation around a compound cylinder for two different small radii b_1 ($b_1/b = 0.5$ in Figs. 6 and 8, and $b_1/b = 0.01$ in Figs. 7 and 9) and two different wave frequencies ($vb = 2$ in Figs. 6 and 7, and $vb = 1$ in Figs. 8 and 9). In both cases, the step along the cylinder is located at the middle of the water depth ($h_1/h = 0.5$). The case $b_1/b = 0.01$ could be considered as a fully submerged, bottom-seated uniform cylinder condition. Figs. 6–9 support the general impression that any alteration in cylinder dimensions should be reflected also on the free surface. The wave run-up on the small diameter which pierces the free surface exhibits a strong variation around the cylinder circumference and the wetted area due to the second-order potential is considerably increased for both wave frequencies considered (Figs. 6 and 8). When the upper diameter of the complex cylinder is very small (Figs. 7 and 9), then it could be assumed as a fully immersed block that obstructs the free water flow. The existence of the underwater body is directly reflected on the water surface and the induced disturbances are more pronounced for high excitation frequencies and smoother for lower frequencies. The location of the cylinder in the wave field is noticeable through the 'bump' on the surface.

Similar conclusions are drawn for deeper water and shorter base ($h/b = 4$, $h_1/h = 0.2$, Figs. 10–12). For better understanding of the numerical predictions for the water surface elevation, the wave patterns in the inner and outer fields due to the second-order potential are shown separately in Figs. 10 and 11. Again it is observed that the particular body geometry leads to an amplification of the wave run-up on the body's surface (compare Figs. 5(b) and 10(b)), despite the fact that the step is very close to the floor. The maximum run-up is located on the lee side only for the higher-frequency case (Figs. 10(b) and (c)), while for the smaller wave frequency the maximum run-up occurs at an azimuthal angle of around 70° (Figs. 12(a) and (b)). It is also interesting to emphasize the extreme disturbances of the water surface around the surface-piercing part of the cylinder. Apparently, the perturbations dominate on a wide area around the body (Fig. 10(a)). Figs. 11(b) and (c), and 12(c) and (d) indicate the location in which a fully immersed cylinder is installed. The maximum values of the wave elevation just above the cylinder are very small, as the cylinder was assumed sufficiently short ($h_1/h = 0.2$). Although the existence of the body inside the fluid domain is not capable of changing drastically the basic characteristics of the wave field, the location of the cylinder may be detected through the disturbances which occur on the free surface.

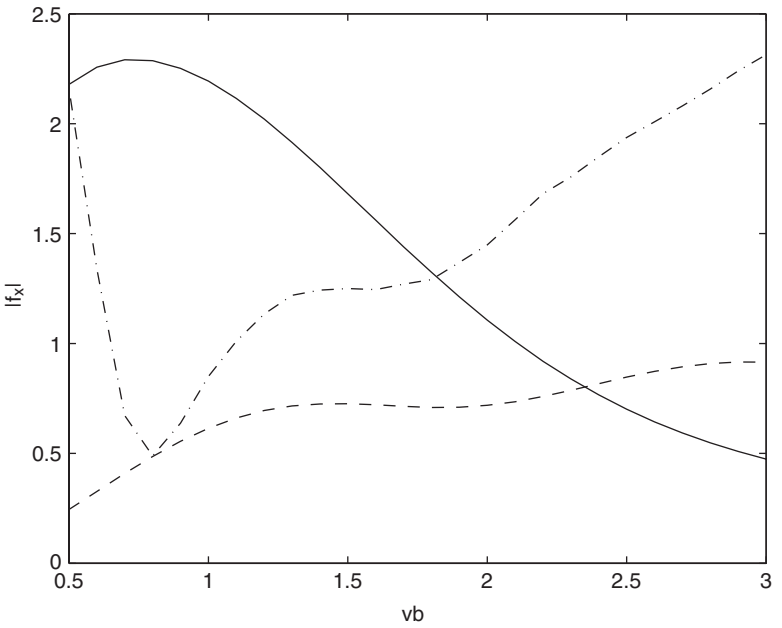

Fig. 15. Amplitudes of the first- and the second-order wave excitation components in the horizontal direction on a bottom-seated, surface-piercing vertical compound cylinder: ———, $|f_x^{(1)}|$; - - - - - - - - -, $|f_{x1}^{(2)}|$; — · — · —, $|f_{x2}^{(2)}|$; $h = b$, $h_1/h = 0.5$, $b_1/b = 0.5$.

The impact of the wave run-up on the compound cylinders examined in Figs. 5–9 is shown in more detail in Figs. 13 and 14. Here, the wave elevation on the circumference of the waterline of the axisymmetric body is plotted against the azimuthal angle. For comparison, Fig. 14 includes also the wave elevation components due to the second-order potential for the equivalent uniform surface-piercing cylinder. In Fig. 13 the linear and second-order counterparts of the wave run-up for a uniform cylinder are plotted. This corresponds to a small excitation frequency $vb = 1$ and indicates that the dominant second-order contribution to wave run-up originates from the second-order potential. It should be mentioned that a different conclusion was drawn for a higher excitation frequency ($vb = 2$, Fig. 2(b)). Also, Fig. 14 shows that a reduction in cylinder diameter may have a negative impact as far as the wave elevation is concerned. In cases of compound surface-piercing cylinders (Figs. 14(a) and (c)), the wave elevation is considerably higher compared that for the equivalent uniform cylinder. For totally immersed bodies however, (Figs. 14(b) and (d)), there is a significant reduction on the surface elevation above the cylinder for higher excitation frequencies. Another feature which should also be noticed is that the use of a compound cylinder with smaller upper diameter results in a very much

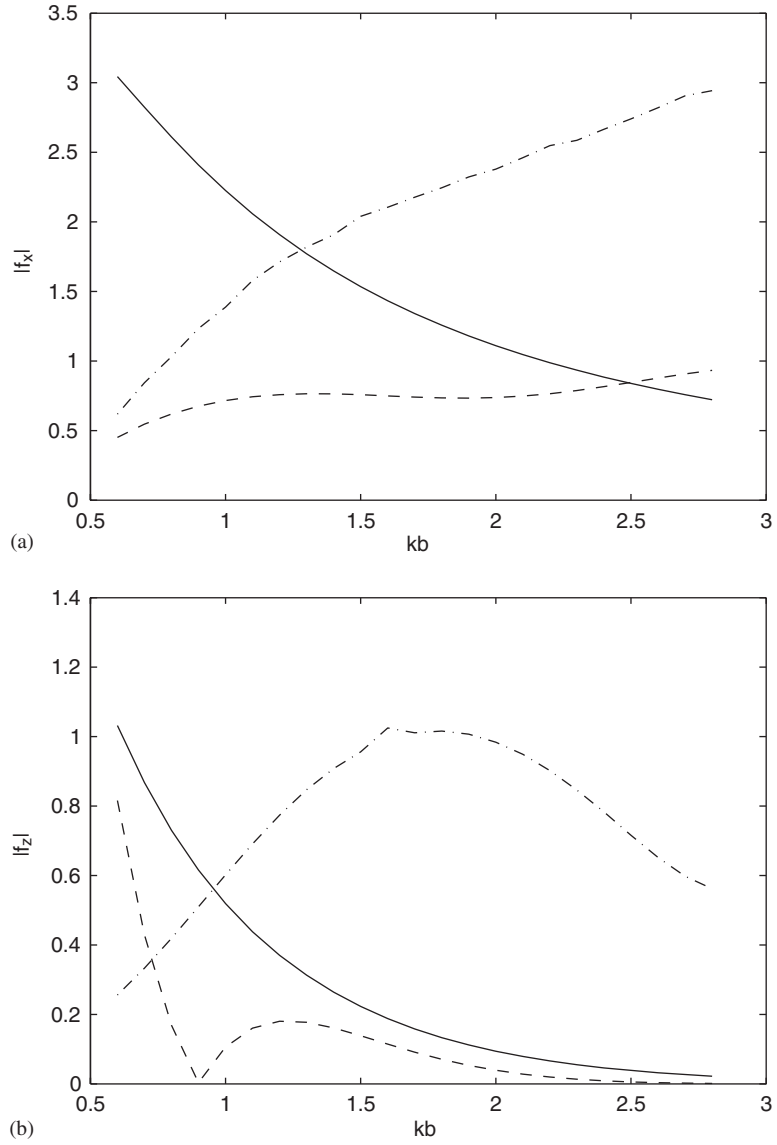

Fig. 16. Amplitudes of the first- and the second-order wave excitation components in the horizontal and vertical direction on a bottom-seated, surface-piercing vertical compound cylinder: ———, $|f_x^{(1)}|$ and $|f_z^{(1)}|$; - - - - - - - - -, $|f_{x1}^{(2)}|$ and $10^*|f_{z1}^{(2)}|$; — · — ·—, $|f_{x2}^{(2)}|$ and $|f_{z2}^{(2)}|$; $h/b = 4$, $h_1/h = 0.6$, $b_1/b = 0.5$. (a) Horizontal force, (b) vertical force.

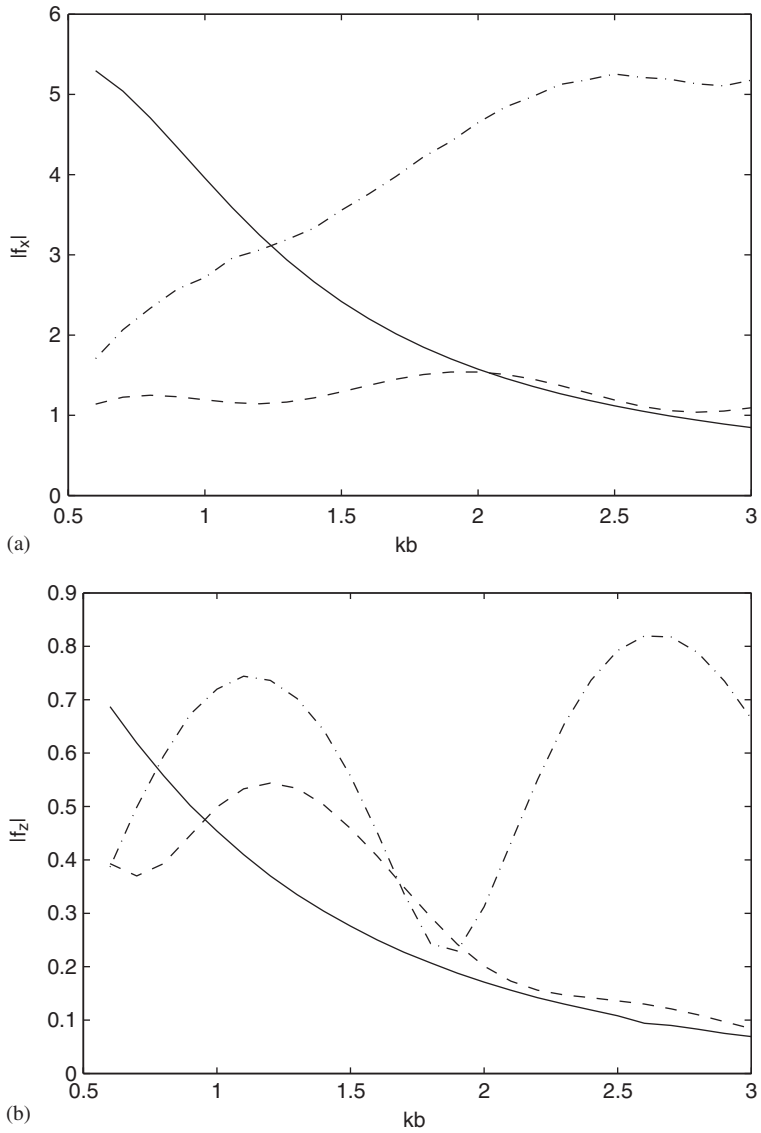

Fig. 17. Amplitudes of the first- and the second-order wave excitation components in the horizontal and vertical direction on a bottom-seated, surface-piercing, vertical compound cylinder: ———, $|f_x^{(1)}|$ and $|f_z^{(1)}|$; ---------, $|f_{x1}^{(2)}|$ and $10*|f_{z1}^{(2)}|$; — · — · —, $|f_{x2}^{(2)}|$ and $|f_{z2}^{(2)}|$; $h/b = 4.0$, $h_1/h = 0.8$, $b_1/b = 0.8$. (a) Horizontal force, (b) vertical force.

higher run-up on the impact point $\theta = 0$, while the corresponding value on the lee is reduced. This can be observed for both wave frequencies examined in Fig. 14(a) and (c).

5.3. Second-order exciting forces

The results for the exciting forces are show in Figs. 15–17. Fig. 16 shows the linear and the oscillating second-order exciting forces acting on a compound bottom-seated cylinder with $h = 4b$, $h_1/h = 0.6$, $b_1/b = 0.5$. The corresponding results for $h_1/h = 0.8$, $b_1/b = 0.8$ are depicted in Fig. 17. The latter case is closer to the uniform cylinder condition. Useful qualitative information about the second-order contribution to the total wave loading can be drawn through these plots. Firstly, the second-order component due to the first-order potential is relatively insignificant. On the

contrary, $f_{x_2}^{(2)}$ and $f_{z_2}^{(2)}$ are very important for higher nondimensional frequencies κb, in which the magnitudes of the first-order forces decay drastically. The horizontal forces $f_{x_2}^{(2)}$, acting on compound cylinders, exhibit apparent similarities with the horizontal forces on the corresponding uniform cylinders. This can be seen by comparing the pairs of Figs. 3(a) and 15, Figs. 3(b) and 16(a) as well as Figs. 3(b) and 17(a). An important feature which must also be noticed is the smoothing of the variation curves through the elimination of the multiple local maxima and minima which characterize the variation of the second-order force $f_{x_2}^{(2)}$ especially for large cylinders (Fig. 3(a)). However, the magnitude of the specific component continues to increase for higher wave frequencies.

The most apparent similitude is observed between the $f_{x_2}^{(2)}$ curves depicted in Figs. 3(b) and 17(a). This can be traced back to the fact that the compound cylinder that is examined in Fig. 17 has large values h_1/h and b_1/b, which in turn implies that the size of the inner field $\boldsymbol{B}$ is sufficiently small. Thus, the small ring shaped field $\boldsymbol{B}$ does not change drastically the pressure field around the cylinder. As a result, the wave loads should be comparable to those acting on the equivalent uniform cylinder.

The vertical forces due to the second-order potential, exhibit a notable variation with respect to the excitation frequency, as manifested in Figs. 16(b) and 17(b). It is interesting to highlight that this variation depends primarily on the size of the small upper part of the axisymmetric body. For $h_1/h = 0.8$ and $b_1/b = 0.8$, two local amplifications occur, while for $h_1/h = 0.6$ and $b_1/b = 0.5$ only one.

6. Conclusions

The second-order diffraction problem around a bottom-seated compound cylinder was investigated. The proposed method was based on a semi-analytical formulation of the total velocity potentials which describe the wave fields defined by the geometry of the structure. It was suggested that the particular solution methodology is appropriate to be used also for a uniform bottom-seated surface-piercing cylinder, as well as for a fully submerged cylinder fixed on the floor.

The method was validated using the numerical predictions reported by other authors in the past. Good agreement was observed with the existing numerical data.

The changes in the fluid field because of the existence of a step on the vertical axisymmetric body were investigated through the wave run-up around the circumference of the waterline and the second-order forces which are exerted on the body. Extensive numerical calculations were presented for completely submerged axisymmetric bodies. The specific case was properly simulated by minimizing the radius of the upper axisymmetric part of the body. The method was implemented for the calculation of the second-order horizontal and vertical forces. It was observed that the horizontal forces due to the second-order potential, acting on vertical compound cylinders, exhibit a similar behaviour to the horizontal forces on the corresponding uniform cylinders. Finally, a notable variation of the second-order vertical forces was detected and it was shown that the number of local maxima for the same wave frequency range depends on the size of the small upper part of the complex cylinder.

Acknowledgements

Support to this work was provided by PYTHAGORAS I Program. The program is co-funded by the European Social Fund 75% and national resources 25%.

Appendix A. Elements of the matrices in Section 2.5

$$W_l = \frac{1}{h}\int_0^h \cosh(2\kappa z) Z_l^{(2)}(z)\,\mathrm{d}z = \left[N_l^{(2)}\right]^{-1/2} \frac{k_l h\cosh(2\kappa h)\sin(k_l h) + 2\kappa h\cos(k_l h)\sinh(2\kappa h)}{(2\kappa h)^2 + (k_l h)^2}, \tag{A.1}$$

$$P_j = \frac{1}{h-h_1}\int_{h_1}^h \cosh(2\kappa z)\, Y_j^{(2)}(z)\,\mathrm{d}z = \frac{\left[M_j^{(2)}\right]^{-1/2}}{[2\kappa(h-h_1)]^2 + [\sigma_j(h-h_1)]^2} \begin{Bmatrix} \sigma_j(h-h_1)\cos(2\kappa h)\sin[\sigma_j(h-h_1)] \\ 2\kappa(h-h_1)\cos[\sigma_j(h-h_1)]\sinh(2\kappa h) \\ -2\kappa(h-h_1)\sinh(2\kappa h_1) \end{Bmatrix}, \tag{A.2}$$

$$V_{jl}^{(2)} = \frac{1}{h-h_1}\int_{h_1}^{h} Y_j^{(2)}(z) Z_l^{(2)}(z)\,\mathrm{d}z = \frac{1}{2}\frac{\left[M_j^{(2)}\right]^{-1/2}\left[N_l^{(2)}\right]^{-1/2}}{[k_l(h-h_1)]^2 - [\sigma_j(h-h_1)]^2}\cdot \left\{\begin{array}{l} -2k_l(h-h_1)\sin(k_l h_1) \\ +[k_l(h-h_1)+\sigma_j(h-h_1)]\sin[k_l h-\sigma_j(h-h_1)] \\ +[k_l(h-h_1)-\sigma_j(h-h_1)]\sin[k_l h-\sigma_j(h-h_1)] \end{array}\right\}, \tag{A.3}$$

$$E_{pl} = (k_p h)\frac{\mathrm{K}'_m(k_p b)}{\mathrm{K}_m(k_p b)}\delta_{pl} - \sum_{j=0}^{\infty}\sigma_j(h-h_1)R'^{2\mathrm{B}}_{mj}(\sigma_j b)V_{jp}^{(2)}V_{jl}^{(2)}, \tag{A.4}$$

$$\begin{aligned} D_l = & -\frac{3}{4}\frac{\mathrm{J}'_m(2\kappa b)}{\sinh^4(\kappa h)}(\kappa h)\ W_l + \frac{3}{8}\frac{\mathrm{J}_m(2\kappa b)}{\sinh^4(\kappa h)}\sum_{j=0}^{\infty}\sigma_j(h-h_1)R'^{(2B)}_{mj}(\sigma_j b)V_{jl}^{(2)}P_j \\ & + \sum_{j=0}^{\infty}\sum_{p=0}^{\infty} Z_p^{(2)}(h)\ V_{jp}^{(2)}V_{lj}^{(2)}\sigma_j(h-h_1)R'^{(2B)}_{mj}(\sigma_j b)\int_1^{\infty}\frac{\xi}{b}Q_m^{(A)}\left(\frac{\xi}{b}\right)G_{mp}^{(A)}\left(1;\frac{\xi}{b}\right)\mathrm{d}\left(\frac{\xi}{b}\right) \\ & - \sum_{j=0}^{\infty} Y_j^{(2)}(h)\sigma_j(h-h_1)R'^{(2B)}_{mj}(\sigma_j b)V_{lj}^{(2)}\frac{\kappa b_1}{\kappa h}\frac{\kappa b_1}{\kappa(h-h_1)}\int_1^{b/b_1}\frac{\xi}{b_1}Q_m^{(B)}\left(\frac{\xi}{b_1}\right)G_{mj}^{(B)}\left(\frac{b}{b_1};\frac{\xi}{b_1}\right)\mathrm{d}\left(\frac{\xi}{b_1}\right), \end{aligned} \tag{A.5}$$

where δ_{pl} is Kroneker's delta.

References

Abul-Azm, A.G., Williams, A.N., 1988. Second-order diffraction loads on truncated cylinders. ASCE Journal of Waterways, Port, Coastal and Ocean Division 14, 436–454.

Abul-Azm, A.G., Williams, A.N., 1989a. Approximation of second-order diffraction loads on arrays of vertical circular cylinders. Journal of Fluids and Structures 3, 17–36.

Abul-Azm, A.G., Williams, A.N., 1989b. Second-order diffraction loads on arrays of semi-immersed circular cylinders. Journal of Fluids and Structures 3, 365–387.

Chau, F.P., Eatock Taylor, R., 1992. Second-order wave diffraction by a vertical cylinder. Journal of Fluid Mechanics 240, 571–599.

Dettman, J.W., 1988. Mathematical Methods in Physics and Engineering. Dover Publications, New York.

Eatock Taylor, R., Hung, S.M., 1987. Second-order diffraction forces on a vertical cylinder in regular waves. Applied Ocean Research 9, 19–30.

Eatock Taylor, R., Huang, J.B., 1997. Semi-analytical formulation for second-order diffraction by a vertical cylinder in bichromatic waves. Journal of Fluid and Structures 11, 465–484.

Ghalayini, S.A., Williams, A.N., 1991. Nonlinear wave forces on vertical cylinders arrays. Journal of Fluids and Structures 5, 1–32.

Hildebrand, F.B., 1962. Methods of Applied Mathematics, second ed. Prentice-Hall Inc., Englewood Cliffs.

Huang, J.B., Eatock Taylor, R., 1996. Semi-analytical solution for second-order wave diffraction by a truncated circular cylinder in monochromatic waves. Journal of Fluid Mechanics 319, 171–196.

Kim, M.-H., Yue, D.K.P., 1989. The complete second-order diffraction for an axisymmetric body. Part 1. Monochromatic incident waves. Journal of Fluid Mechanics 200, 235–264.

Kim, M.H., Yue, D.K.P., 1990. The complete second-order diffraction solution for an axisymmetric body. Part II: bichromatic incident waves and body motions. Journal of Fluid Mechanics 201, 557–593.

Lighthill, J., 1979. Waves and hydrodynamic loading. Proceedings of the Second International Conference on Behaviour of Offshore Structures vol. 1, pp. 1–40.

Liu, Y.H., Kim, M.H., Kim, C.H., 1995. The computation of second-order mean and double-frequency wave loads on a compliant TLP by HOBEM. International Journal of Offshore and Polar Engineering 5, 111–119.

Loken, A.E., 1986. Three-dimensional second-order hydrodynamic effects on ocean structures in waves. Report UR-86-54, Department of Marine Technology, University of Trondheim, Norway.

Malenica, S., Eatock Taylor, R., Huang, J.B., 1999. Second-order water wave diffraction by an array of vertical cylinders. Journal of Fluid Mechanics 390, 349–373.

Mavrakos, S.A., Koumoutsakos, P., 1987. Hydrodynamic interaction among vertical axisymmetric bodies restrained in waves. Applied Ocean Research 9, 128–140.

Mavrakos, S.A., Peponis, V., 1992. Second-order sum and difference wave loads on axisymmetric bodies restrained in irregular waves. Proceedings of the Second International Offshore Polar Engineering Conference vol. III, pp. 546–553.

Mei, C.C., 1983. The Applied Dynamics of Ocean Surface Waves. Wiley, New York.

Molin, B., 1979. Second-order diffraction loads upon three dimensional bodies. Applied Ocean Research 1, 197–202.

Moubayed, W.I., Williams, A.N., 1994. The second-order diffraction loads and associated motions of a freely floating cylindrical body in regular waves: an eigenfunction expansion approach. Journal of Fluids and Structures 8, 417–451.

Moubayed, W.I., Williams, A.N., 1995. Second-order hydrodynamic interactions in an array of vertical cylinders in bichromatic waves. Journal of Fluids and Structures 9, 61–98.

Ogilvie, T.F., 1983. Second-Order Hydrodynamic Effects on Ocean Platforms. International Workshop Ship and Platform Motion, Berkeley, CA, USA, pp. 205–265.

Press, W.H., Flannery, B.P., Teukolsky, S.A., Vetterling, W.T., 1986. Numerical Recipes. Cambridge University Press, Cambridge.

Rahman, M., Bora, S.N., Satish, M.G., 1999. A Note on second-order wave forces on a circular cylinder in finite water depth. Applied Mathematics Letter 12, 63–70.

Teng, B., Kato, S., 1999. A method for second-order diffraction potential from an axisymmetric body. Ocean Engineering 26, 1359–1387.

Williams, A.N., Abul-Azm, A.G., Ghalayini, S.A., 1990. A comparison of complete and approximate solutions for second-order diffraction loads on arrays of vertical circular cylinders. Ocean Engineering 17, 427–445.